SYNTHESIS AND CHARACTERIZATION OF PHOSPHORESCENT
STRONTIUM ALUMINATE COMPOUNDS

by
ANNA VANYA ULUÇ

Submitted to the Graduate School of Engineering and Natural Sciences
in partial fulfillment of
the requirements for the degree of
Master of Science

Sabancı University
Spring 2008

SYNTHESIS AND CHARACTERIZATION OF PHOSPHORESCENT

STRONTIUM ALUMINATE COMPOUNDS

APPROVED BY:

Assist Prof. Cleva Ow-Yang …………………........................

(Dissertation Supervisor)

Assoc.Prof. Mehmet Ali Gülgün …………………...................

Prof.Dr. Alphan Sennaroğlu…………………...........................

Assoc.Prof. Alpay Taralp   …..…………………...................

DATE OF APPROVAL: …………………………..

SYNTHESIS AND CHARACTERIZATION OF PHOSPHORESCENT
STRONTIUM ALUMINATE COMPOUNDS

Anna Vanya Uluç

MAT, M.Sc. Thesis, 2008

Thesis Supervisor: Asst. Prof. Cleva Ow-Yang

ABSTRACT

The emission of light after the excitation source is switched off is known as phosphorescence. Phosphorescence occurs when suitable elements with active electronic configuration are doped into certain host materials. For an efficient phosphorescence emission (long after glow time and high intensity), both the dopant ion and the host material are critical. Strontium aluminates, such as $SrAl_2O_4$, $SrAl_4O_7$, $SrAl_{12}O_{19}$, have gained attention for the last two decades due to their phosphorescence behavior upon doping with rare earth elements such as Eu, and Dy. These phosphorescent materials are superior to other materials of this kind as they have long after glow times with high quantum efficiency; they are easy to produce with alternating methods and are low cost materials.

The focus of this thesis is on the different stoichiometric compounds of strontium aluminates with the dopants Eu^{2+}, Dy^{3+}, and boron. Eu^{2+} introduces phosphorescence whereas Dy^{3+} is used to increase the after glow time. Boron on the other hand improves the crystallinity, and also the after glow time. The general aim of this thesis is to develop materials with long after glow duration i.e more than one hour. A modified version of the Pechini process is proposed in order to accomplish the objective. The proposed procedure is one step ahead from the previous studies as it is an easy, low-temperature and low-cost method. Moreover, by the proposed method, strontium aluminate compounds can be incorporated with up to 30% boron without disturbing the crystal lattice and hence without lowering the crystallinity. These advantages are also verified experimentally.

FOSFORESANS ÖZELLİKLİ STRONSİYUM ALÜMİNAT BİLEŞİKLERİNİN SENTEZİ VE KARAKTERİZASYONU

Anna Vanya Uluç

MAT, Yüksek Lisans Tezi, 2008

Tez Danışmanı: Yrd.Doç.Dr. Cleva Ow-Yang

ÖZET

Fosforesans tahrik kaynağı kapalı olduğunda ışık yayınımının halen devam etmesi durumuna verilen genel addır. Fosforesans, aktif elektronik konfigürasyona sahip uygun elementlerin uygun kristal yapılı malzeme içerisine katkılandırılmasıyla meydana gelir. Verimli bir fosforesans yayınımı için (uzun yayınım süresi ve yüksek ışık şiddeti) hem katkılandırma iyonu hem de matris malzemesi önem taşır. $SrAl_2O_4$, $SrAl_4O_7$, $SrAl_{12}O_{19}$, gibi stronsiyum alüminatlar fosforesans özellikleri nedeniyle geçtiğimiz 20 sene içerisinde dikkat çekmişlerdir. Bu malzemeler uzun süreli yayınımları, yüksek kuantum verimlilikleri, kolay imal edilebilirlikleri ve düşük maliyetleri nedeniyle diğer malzemelerden daha ön plana çıkmışlardır.

Bu tezin odağı değişik stokiyometrik oranlardaki stronsiyum alüminat bileşiklerini Eu^{2+}, Dy^{3+} ve boron ile katkılandırılmasıyla elde etmektir. Eu^{2+} malzemeye fosforesans özelliğini katarken, Dy^{3+} yayınım süresini artırıcı rol oynar. Boron ise kristal yapıyı teşvik eder ve yayınım süresini artırır. Bu tezin genel amacı ise yayınım süresi yüksek (bir saatten fazla) fosforesans malzemeler geliştirmektir. Bu amaçla, orijinal Pechini süreci üzerinde değişiklikler yapılmış ve yeni bir metod önerilmiştir. Önerilen bu metod kolay uygulanışı, düşük sıcaklıkları gerektirmesi ve maliyetinin düşük olması nedeniyle önceki çalışmalardan daha verimlidir. Ayrıca bu metotla stronsiyum alüminat bileşiklerine %30'a kadar boron katkılandırılabilmektedir. Bahsedilen bu avantajlar deneysel çalışmalarla ispatlanmıştır.

ACKNOWLEDGEMENTS

First and foremost, I would like to thank my thesis supervisor Dr. Cleva Ow-Yang for her support and encouragement on this thesis study. Our technical discussions guided me through each and every step of this work. I would also like to express my special thanks to my co-advisor Dr. Mehmet Ali Gülgün, for his valuable advices about this study, for his guidance and endless optimism during the years. With the supervision of Dr. Ow-Yang and Dr. Gulgun, I believe I took the first steps of an academic career, which will always be appreciated.

I am grateful to my committee members Dr. Alphan Sennaroglu, Dr. Alpay Taralp, and Dr. Mehmet Yildiz for their invaluable suggestions about this thesis.

I wish to express my gratitude to the whole staff of the Materials Science and Engineering Program of Sabanci University for their help and contribution.

Kind helps of Dr. Vesna Srot on the ELNES measurements are very much appreciated. Also, I would like to thank Dr. Peter A. van Aken for providing the necessary facilities for these measurements.

My dear friends and colleagues Seren Yüksel, Özge Malay, Gülay Bozoklu, Emre Fırlar, Cahit Dalgıçdir, Eren Şimşek, Deniz Turgut, Gökhan Kaçar, Çınar Öncel and Ahu Gümrah Dumanlı were always there for me during my time at Sabanci University. They have motivated me with their friendship whenever I felt down, which will always be remembered. I wish to express my warmest thanks to Emre Özlü not only for his great contribution on the formatting of this thesis, but also for his belief in me. I am also thankful to my cousin and dear friend Natali Cizmeciyan for her support and friendship.

My special thanks belong to Ali Burak for being in my life during these years with his loving support and understanding.

Last but not the least, I would like to thank my parents Hilda and Aydın Uluç, my grandmother Alis Serop and my brother Artür Uluç for their endless support for the past 25 years. They are the true motivation source of this study for which I am, and will always be grateful.

TABLE OF CONTENTS

LIST OF FIGURES

LIST OF TABLES

LIST OF ABBREVATIONS

CA	Citric acid
CB	Conduction band
CL	Cathodoluminescence
EDS	Energy dispersive X-ray spectroscopy
EDX	Energy dispersive X-ray
EELS	Electron energy loss spectroscopy
EG	Ethylene glycol
ELNES	Energy Loss Near Edge Spectroscopy
EXELFS	Extended electron-energy loss fine structure
FCC	Face centered cubic
FL	Fluoroscence
JDOS	Joint density of states
PL	Photoluminescence
SEM	Scanning electron microscopy
TEM	Transmission electron microscopy
TL	Thermoluminescence
UV	Ultraviolet
VB	Valence band
XRD	X-ray diffraction
ZLP	Zero loss peak
E_g	Band gap energy
λ	Wavelength
E_c	Critical ionization energy
$(SrO)_x(Al_2O_3)_y$	S_xA_y

CHAPTER 1.   INTRODUCTION

When the water of oceans or seas is disturbed during the night, sometimes it is possible to see blue-green sparkles. These colorful lights make scuba diving an attractive sport during the night. The light is due to bioluminescent planktons named noctiluca scintillans, which stands for "night lights". When the plankton population is large enough, a continuous glow can be observed. Although commonly known as phosphorescent water, the term is a misnomer since the light is produced chemically in short bursts.

Nature is full of self-luminescent living organisms and noctiluca scintillans are only one of them. As it is the case in many other discoveries in science, humans have been trying to imitate the luminescence behavior of self-luminescent organisms for many years. Obviously, luminescence becomes important when it is observed at night. Thus, producing "night lights" has been one of the main focuses of manmade luminescent materials.

The concept of extended glowing in the dark is known as phosphorescence. To be more specific, while luminescence is a general term for the emission of radiation in the visible part of the electromagnetic spectrum, the emission of light after the excitation source is switched off is known as phosphorescence. Phosphorescence is identical to fluorescence except that fluorescence (FL) is the "finite" emission (*i.e.* ms to ns lifetime) after excitation by an external source, while phosphorescence is the afterglow extending many timescales over the FL lifetime.

Fluorescent materials find major application areas in fluorescent lightning via fluorescent lamps (ultraviolet to visible), display devices via cathode ray tubes (electron

impact to visible), and scintillators (X-Rays and γ-Rays to visible). The delayed emission and hence phosphorescent materials (phosphors) find use in luminous paints, clocks and watches, emergency lightning, exit signs etc. In fact, whenever there is no source of light but still light is needed, phosphors serve the purpose well.

There are many materials that are used as phosphors, and new materials with phosphorescent activity are being discovered regularly. Phosphorescence occurs when suitable elements with active electronic configuration are doped into certain host materials. For an efficient phosphorescence emission (long after glow time and high intensity), both the dopant ion and the host material are critical. The host material is important, since it defines the environment of the dopant ion, and determines the physical behavior of the material to external disturbances. On the other hand, the dopant ion will determine the color of the emission and also the time of the after glow by introducing or shifting the position of trap states in the forbidden energy band gap of the material.

The following are some of the widely used inorganic phosphor materials: simple oxides such as CaO, ZnO, Y_2O_3; silicates such as $CaSiO_3$, Ba_2SiO_4, $BaMg_2Si_2O_7$; phosphates such as YPO_4, CaP_2O_6, SrP_2O_7; borates such as YBO_3, CaB_2O_4, SrB_4O_7; aluminates such as $LiAlO_2$, $YAlO_3$, $MgAl_2O_4$, $CaAl_2O_4$, $BaAl_2O_4$, $CaAl_4O_7$, $Y_4Al_2O_9$, $BaMgAl_{10}O_{17}$; molybdates and tungstates such as $CaMo_4$ and Sr_3WO_6; halides such as $CaCl_2$, SrF_2, ZnF_2; sulfates such as $CaSO_4$, $SrSO_4$, ZnS-type sulfides and CaS-type sulfides. There are many different dopant ions, which are incorporated into different host materials. Some of the widely used dopant ions are Bi^{3+}, Cd^{2+}, Cu^+, Ga^{3+}, S, Er^{3+}, Pb^{2+}.

Host lattices, strontium aluminates, such as $SrAl_2O_4$, $SrAl_4O_7$, $SrAl_{12}O_{19}$, and the dopants Eu^{2+}, Dy^{3+}, and boron are being used for phosphorescent materials for the last two decades. They have several advantages such as they have long after glow times with high quantum efficiency; they are easy to produce with alternative methods and are low cost materials. The focus of this thesis is on the different stoichiometric compounds of strontium aluminates with the dopants Eu^{2+}, Dy^{3+}, and boron. The general aim on the other hand is to develop materials with long after glow times, *i.e* more than one hour, which requires a clearer understanding of the relationship between the atomic and electronic structure with the optical properties.

1.1. Literature Review

Rare earth (Eu, Dy) doped strontium aluminates, $SrAl_2O_4$ (SA), $SrAl_4O_7$ (SA$_2$), $SrAl_{12}O_{19}$ (SA$_6$), $Sr_3Al_2O_6$ (S$_3$A) are new and efficient phosphorescent materials that have gained attention for the past twenty years due to being able to replace the use of sulfide phosphors that are doped with radioactive materials and used in luminous watches, clocks, paints, emergency exit signs, *etc.* [1,2]. Other non-radioactive element doped phosphorescent materials such as ZnS:Cu do not luminesce with as high intensity and length of afterglow desirable for these applications[2,3]. The addition of Eu in its trivalent state generates only fluorescence, whereas the reduction of Eu^{3+} to Eu^{2+} enables phosphorescence [4,5]. Thanks to the reduction, Eu^{2+} could also replace Sr^{2+} in the crystal lattice, while preserving local charge neutrality. Dy^{3+} is known to extend the phosphorescence time. Boron, usually added to the system as a flux for processing by solid-state reactions, has also been reported to extend the phosphorescence time [4,6,7].

There are several possible routes for synthesizing the strontium aluminate compounds. The conventional method is the solid-state reaction, in which a mixture of the SrO and Al_2O_3 compounds are solidified from their liquid states. According to the phase equilibrium diagram of the SrO-Al_2O_3 system [8], which can be seen in Figure 1.1, these reactions require temperatures of 1750°C to 1950°C.
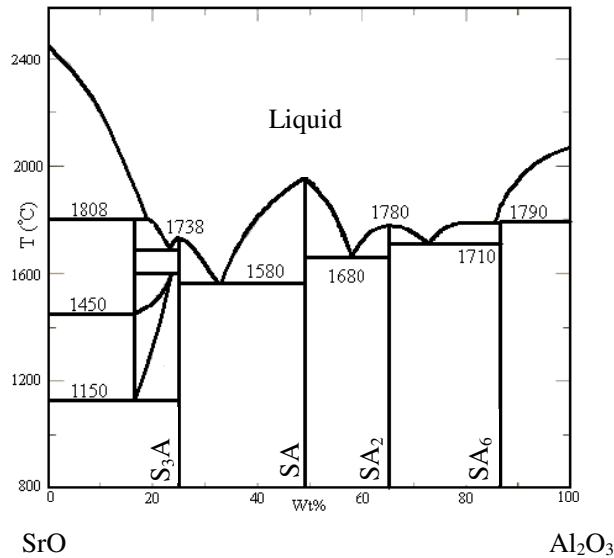
Figure 1.1 Binary phase diagram of SrO-Al_2O_3 showing stoichiometric compounds of strontium aluminates

In this method, $SrCO_3$ and Al_2O_3 are used as the starting materials. Europium is added to the system as Eu_2O_3. The chemical reactions rely on the diffusion of atoms or ions, and thus high temperatures are necessary to enable the diffusion. Usually, before the calcination process at high temperatures, ball milling is performed under either wet or dry ambient to distribute the powders homogeneously. Adding boron as a flux agent to the system in the form of H_3BO_3 or B_2O_3 could reduce the calcination temperature down to 1300˚C, but not any lower due to the decomposition of $SrCO_3$ at 1258˚C [9-14].

Lower temperature methods exist to ease the production of strontium aluminate compounds. There are several methods proposed by different groups. These include the microwave route [15], sol-gel method [16], combustion synthesis method [17,18], citric acid precursor route [19], and spray dryer method [20]. Among these, Tang *et al.* reported the successful production of SA:Eu,Dy by sol-gel processing, comparing their results to a reference material obtained by solid-state reaction, as well as to the JCPDS data. However, their XRD spectra show additional peaks that indicate the presence of additional phases in their sol-gel synthesized powders. In addition, the crystallinity of their powders is low, although they have used temperatures as high as 1400˚C. Moreover, the XRD spectrum of the SA_6 powders synthesized by Singh *et al.* via combustion showed that some of the peaks had just emerged at 500˚C, suggesting that further firing was necessary at higher temperatures in order to reduce the amorphous phase content.

The Pechini process has been used since the 1960's to produce ceramic powders at low temperatures, due to being a cost-effective and more efficient process compared to the conventional solid-state method. The Pechini process is a solution polymerization technique, in which crystallization occurs with metal ions chelated by organic acids [21]. The metal ions, which are attracted to the relatively negatively charged zones of organic acids, are trapped by polyesterification of those organic acids with the addition of polyhydroxyl alcohols. The metal ions are well dispersed in solution; by reducing the distance between metal ions, it becomes easier to produce a homogenous, single-phase material at lower temperatures, compared to the conventional solid state method.

1.2. Objective

In this thesis our aim is to develop phosphorescent materials with long after glow times and high emission intensity. As reviewed in the previous chapter, there are several proposed methods for this process. However as discussed above, the previously proposed methods have several disadvantages such as long processing times, high-temperature needs, complicated procedures and relatively high cost solutions. In order to overcome these difficulties we propose an enhanced synthesis process, which is a modified version of the Pechini method. The proposed method is not only cost-effective but also very simple to apply. The other advantage of the proposed method is that, it is a low temperature method.

As for the materials used in this study, strontium aluminates, such as $SrAl_2O_4$, $SrAl_4O_7$, $SrAl_{12}O_{19}$, were selected as the host lattices. Also, Eu^{2+}, Dy^{3+}, and boron were used as the dopants. This is due to the fact that the combination of these host and dopants are superior to other materials used for phosphorescence purposes as they have long after glow times with high quantum efficiency; they are easy to produce with alternative methods and are low cost materials. The focus of this thesis is on the different stoichiometric compounds of strontium aluminates with the dopants Eu^{2+}, Dy^{3+}, and boron.

Because the overall goal is to understand the mechanisms of extended phosphorescence, determining the synthesis of a suitable model material was merely the first step leading to investigating the structure-property relationship. Characterization of the material enabled us to start modeling the electronic and atomic structure features that controlled the extent of afterglow. Conventional characterization techniques could be used to obtain phase composition information. However, elucidating the role of boron in the host crystal structure required the development of ELNES fingerprinting techniques.

CHAPTER 2.   THEORY

In this chapter, the background and basic theory on the electronic transitions, luminescence phenomena and the band structure of materials are presented in detail.

2.1.   Electronic Energy Levels and Transitions

To start from the beginning, electronic transitions within a given atom can give rise to color through the emission of light. The atomic emission of sodium is a well known example of the yellow color of the flame of this elemental compound. The ground level electronic configuration of Na is $1s^2 2s^2 2p^6 3s^1$, and the outermost electron is the $3s^1$ electron. The ground state of this valence electron has two closely spaced energy levels above it, one at 2.105 eV and the other one 2.103 eV above the $3s^1$ level. The corresponding wavelengths of light of these energies are 589.1 and 589.6 nm, where the longer wavelength corresponds to the lower energy emission shown in Figure 2.1. These wavelengths of light emitted from excited sodium atoms at about 590 nm, correspond to the yellow part of the visible light spectrum. Thus, when a sodium-containing material is heated in a flame so that $3s^1$ electrons are excited to the 3p levels, the electrons can then return to the ground state while emitting yellow light. This type of emission is a simple model, where only the excitation of the valence electrons is necessary to produce the emission colors. However, when the valence electrons of

isolated atoms combine with another atom to form chemical bonds, the ground state energy of the atom is lowered, and much more energy is required to promote them to excited states. In many compounds, the outermost electrons are stabilized by chemical bonding in this manner, requiring energy in the UV region for excitation. No visible color is associated with absorption and emission from these materials, but still they do absorb UV light. One exception is compounds containing transition metals with incomplete d-shells. The excitation of these valence electrons can fall in the visible region of the spectrum, and these compounds can have different colors. This is also true for compounds containing transition metal impurity ions.

excited states

3p   2.105 eV

3p   2.103 eV

ground state

3s
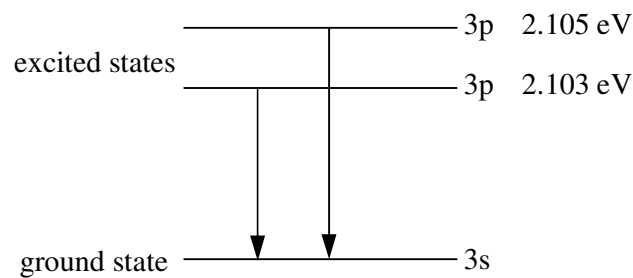
Figure 2.1 The electronic energy levels of Na showing the transitions, which correspond to yellow color in the visible region.

All electronic energy levels are sensitive to their environment. An ion in the electrical potential field in a crystal (*i.e.*, in a crystal field) has different energy levels from that of the free ion. Because a dopant ion interacts with the crystal field of its host lattice, de-excitation of the host electrons can give rise to observable colors, thus providing information on the electronic configuration of the ion itself. An example to this phenomenon is ruby. When Al_2O_3 is doped with Cr^{3+} to replace Al^{3+} in the structure, the changes in the crystal field engender the absorption of violet and yellow-green light. Thus ruby appears red due to the subtractive cause of color [22].

In an isolated atom, the electrons occupy a ladder of sharp energy levels. If another atom approaches the first, the outer electron clouds will interact, and the result is that the single energy level will split up into two, one at a higher energy and one at a lower energy, as can be seen in Figure 2.2. Four atoms will give four energy levels. This process can be continued indefinitely. As each atom adds to the cluster, the number of energy levels in the high energy and low energy groups increase. At the same time, the spacing between the energy levels in each group decreases. Ultimately, when a large number of atoms are brought together, as in a solid, the energy levels in both the high

7

energy and low energy groups become very close and they are named as energy bands [23].
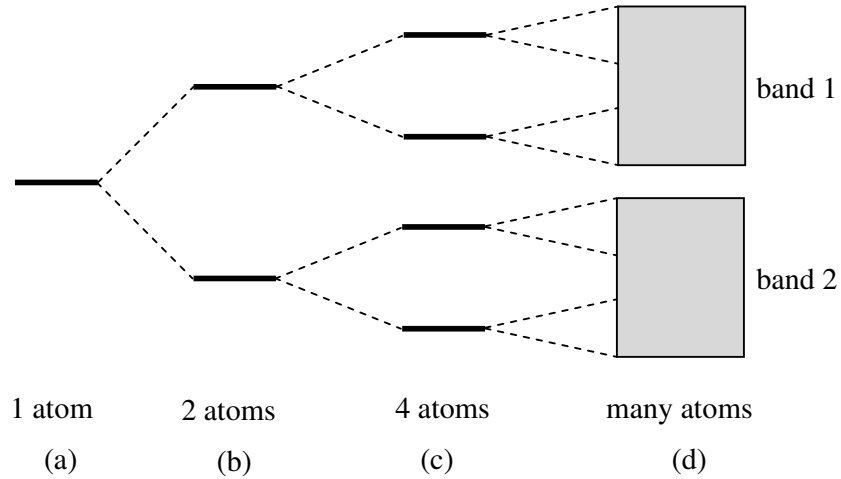
Figure 2.2 The formation of energy band. (a) Isolated atom (b) Energy levels in a diatomic molecule. (c,d) Energy levels of multi atoms

The details of the band structure of a crystal depend upon both the geometry of the structure and the degree of interaction of the electron energy levels. When the interaction is large, typically for the outer orbitals of closely spaced, large atoms, the bands are broad. When the interaction is less, such as the case for the inner electron orbitals of atoms, which are further apart, the width of each band is rather narrow. The electrons in the solid fill the bands from the lowest energy to the highest [23].

Insulators have an empty upper energy band, while the lower energy band is completely occupied by electrons (Figure 2.3*a*). Moreover, the energy gap between the top of the filled band and the bottom of the empty band is quite large. The filled energy band is called the valence band (VB) and the empty energy band is called the conduction band (CB). The energy difference between the top of the valence band and the bottom of the conduction band is called the band gap [23].

Intrinsic semiconductors have a similar band picture to insulators except that the separation of the empty and filled energy bands is small (see Figure 2.3.b). The band gap must be such that some electrons have enough energy to be transferred from the top of the valence band to the bottom of the conduction band at room temperature. Each electron transferred will leave behind a vacancy in the valence band. These vacancies behave as positively charged electrons. They are named as holes. Therefore, each time

an electron is removed from the valence band and transferred to the conduction band, two mobile species are created; an electron and a hole [23].

Metals are defined as materials in which the uppermost energy band is only partly filled which can be found in Figure 2.3.c. The highest energy attained by electrons in this band is called the Fermi Energy.
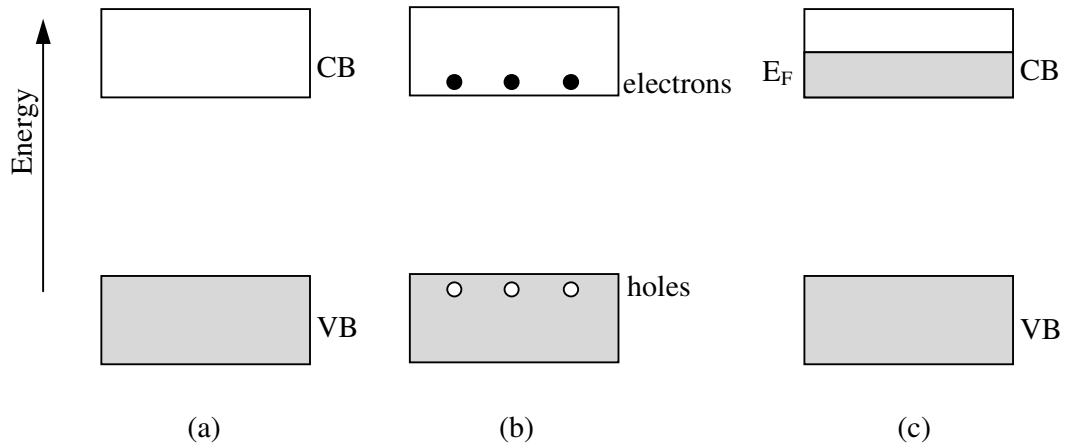
Figure 2.3 Schematic illustration of the energy bands in (*a*) an insulator, (*b*) an intrinsic semiconductor and (*c*) a metal.

2.2. Luminescence – Theory and Classes

In this section, a short theory of luminescence will be presented, building on the previously mentioned band theory of atoms, molecules and solids. Also, the classification of luminescence processes will be given.

2.2.1. Theory of Luminescence

Luminescence is the general term describing the emission of electromagnetic radiation in the visible region of electromagnetic spectrum by relatively cool bodies, as opposed to incandescence, which applies to light emission from hot bodies [24, 25]. The emission is usually independent of the nature of the excitation, which is the pre-

requisite to the emission, and lies in a region where the substance is non-absorbing. The emission of radiation results when a material adjusts itself from an excited to a ground state. Luminescence from inorganic solids is normally dominated by extrinsic factors such as impurities, defects, and excited states of isolated atoms and ions. Impurities or defects in structure responsible for emissions are named activators. The electronic states involved in the luminescence due to impurities can be either the energy levels of the impurity ion perturbed by the crystal field or the band structure of the crystal disturbed by the impurity. Transitions may be divided into two as radiative transitions and non-radiative transitions.

Radiative Transitions: Luminescence may involve radiative electronic transitions emitting a photon, when an electron drops from an upper to the lower energy level of either intrinsic band state or impurity levels. Radiative transitions may be of different types: (i) Transitions between intrinsic band and impurity state, which may occur between a deep impurity level and one of the bands (*i.e.* CB to acceptor or to donor to VB) with momentum conservation even in indirect gap materials. (ii) Band-to-band transitions involving free electrons and holes. Such transitions usually occur in direct-gap materials, such as II-VI compounds, between the CB and the VB with conservation of momentum. In case of indirect gap materials, phonon emission is likely to occur (see Figure 2.4). (iii) Transitions between donor (activator) and acceptor (co-activator) levels. Activator atoms occupy Group II cation lattice sites and behave as deep acceptor levels below the CB edge. (iv) Transitions occurring within the impurity (luminescent) center without ionization. The electron is not excited from the center to transition to the CB; instead it returns to the ground state exhibiting a narrow spectrum characteristic of an atomic transition.
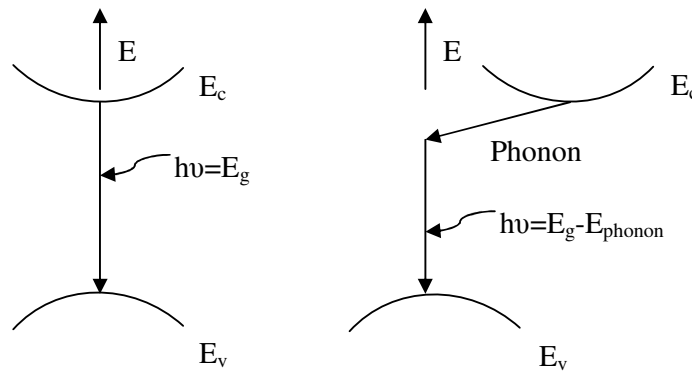
Figure 2.4 Transitions from conduction to valence band for (a) direct gap and (b) indirect gap materials

10

Non-radiative Transitions: Several possible mechanisms leading to non-radiative transitions, competing with the radiative ones, and adversely affecting the luminescence efficiency, can be described as: (i) Generation of phonons due to thermal vibrations. (ii) Recombination at surface states, dislocations, grain boundaries, pores etc., by losing the excess energy through step-wise transitions, so called cascade-process, between narrowly spaced levels existing throughout the forbidden energy gap in the crystal joining CB and VB, emitting one single phonon at each step. (iii) All the defects sites may not act as recombination centers to allow the carriers to recombine radiatively. (iv) Auger process, in which the energy lost by the captured carrier excites another nearby carrier in the crystal and may give rise to non-radiative loss of energy. The other carriers can return to a lower energy state by multiple phonon emission.

Every luminescence process consists essentially of three stages: (i) the excitation or absorption, (ii) storage of excitation energy which determines the average duration of luminescence following the removal of the excitation source, (iii) the emission. It may be noted that if the luminescence exists for $\sim 10^{-8}$ seconds, which is the life time of the atoms in the excited state, or less this is termed "fluorescence" whereas the delayed luminescence is called "phosphorescence".

The absorption of energy in an insulator occurs by the following possible processes: (i) excitation of crystal vibrations (lattice absorption), (ii) formation of excitons (electron in the CB paired with a hole in the VB), (iii) excitation of electrons across gap from VB to CB (intrinsic absorption), (iv) excitation of the impurities and structural defects present in the solid from ground states to their excited states, *etc*.

A plot of absorption coefficient *vs*. energy gives rise to the absorption spectrum of the material, which relates to the transitions corresponding to the creation of a free hole and a free electron. In an idealized absorption spectrum, there is a cut off at the minimum energy corresponding to the band gap for the transition between the VB and the CB. The corresponding wavelength is called the "absorption edge" of the host lattice. The typical absorption and emission spectra can be seen in Figure 2.5. The electronic states originating from impurities and structural defects, and responsible for luminescence emission, contribute optical absorption bands on the long wavelength side of the fundamental absorption edge of a perfect crystal.
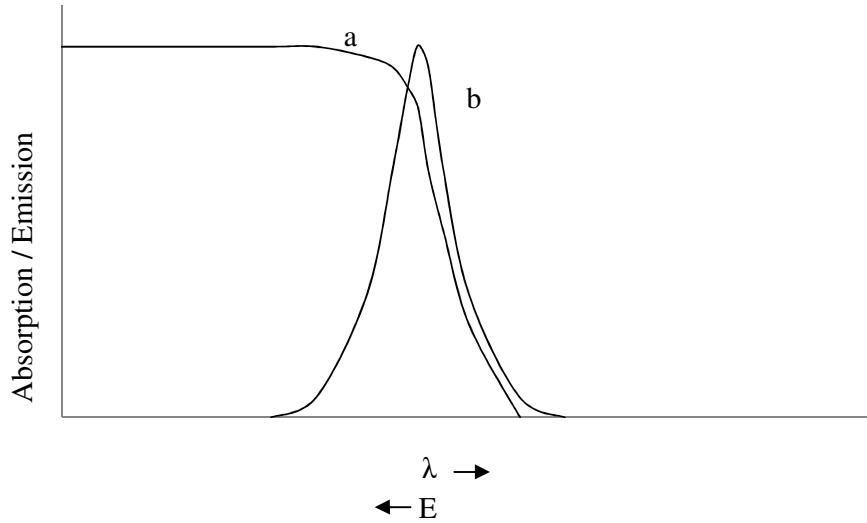
Figure 2.5 Representative (a) absorption and (b) emission edge spectra.

The position of the activator and co-activator levels in the forbidden energy gap region, and the energy transitions involving radiative emission can be represented basically in terms of three general models that are summarized in Figure 2.6.
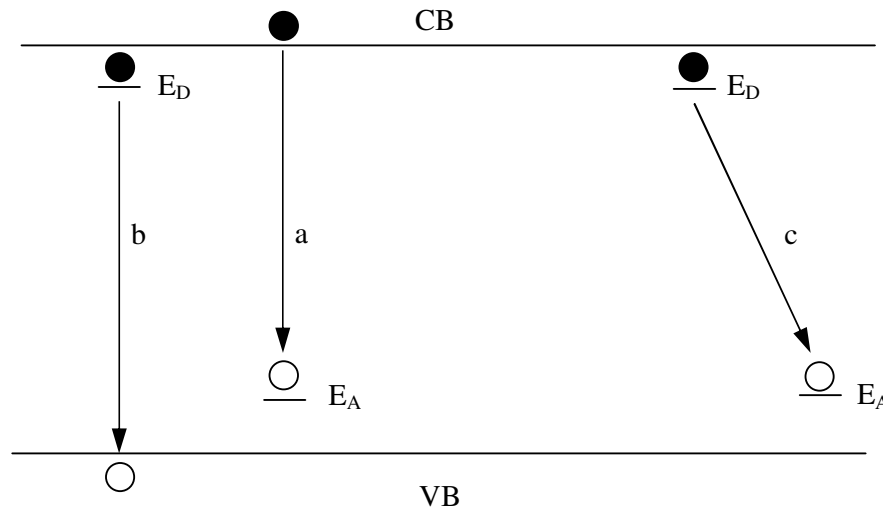
Figure 2.6 Transitions involving radiative emission. (a) defect band transition of Schön-Klasens model (b) defect band transition of Lambe-Klick model (c) donor-acceptor pair transition of Prener-Williams Model

The Schön-Klasens model (see Figure 2.6.a) describes luminescence as a result of radiative recombination of an electron from the CB with a localized acceptor above the VB. The Lambe-Klick model (see Figure 2.6.a) describes the luminescent transition of a free hole recombining with a trapped electron at a level below the CB. The Prener-Williams (see Figure 2.6.c) accounts for a localized radiative association of activator

12

and co-activator. Although these simple models are good assumptions, they are not always complete for an understanding of the nature of luminescence centers and radiative transitions.

2.2.2. Classes of Luminescence

Depending on the type of the excitation process, it is customary to classify luminescence into several groups. Photoluminescence (excitation by photons), cathodoluminescence (by cathode rays or energetic electrons), electroluminescence (by an electric field), triboluminescence (subject to mechanical forces, i.e. grinding), chemiluminescence (by utilizing chemical reaction energy) are types of luminescence processes. However, in thermoluminescence, the heat of irradiation is not an excitation agent but only a stimulant [24].

Photoluminescence: Photoluminescence (PL) is a very useful tool in examining excitation transport in molecular solids, regular crystals or disordered system, and is a well established technique to study optical properties and electronic structure of semiconductors. The spectral features from PL measurements can provide valuable information concerning the type of defects and impurities in semiconductors, while the overall PL intensity is determined by the quantum efficiency of the material together with surface recombination velocity.

Fluorescence (FL), as a type of PL, refers to the instantaneous emission of radiation after the excitation by some other external radiation. The radiation emitted has a longer wavelength (lower energy) than the exciting radiation. The "missing energy" is lost via non-radiative transitions, which increase lattice vibrations, resulting in a heating of the material.

Phosphorescence, which is another type of photoluminescence, is the delayed emission of radiation, but is otherwise identical to fluorescence. The delay can vary milliseconds to hours or days. In this phenomenon, the absorbed energy can be thought of as stored in a reservoir from which it slowly leaks.

Cathodoluminescence: In a luminescent material, the type of cathodoluminescence (CL) emission observed is more or less the same as that of PL, the only difference lies in the excitation mechanism since photon absorption will not excite

luminescence unless it lies in the absorption region of the material, whereas the electron absorption is strong irrespective of their energy. Many crystalline phosphors which are not luminescent under photo-excitation exhibit emission under the excitation by energetic electrons and the whole crystal lattice is strongly disturbed, and even electrons of the inner atomic shells of the luminescent centers are excited.

Thermoluminescence: The phenomenon of thermoluminescence (TL) has become an established and as a sensitive technique for observing changes in defect concentrations in phosphorescent materials. Defects in an insulating solid usually form electron trapping states, within the forbidden energy gap, whose densities can be monitored by TL observations to as low as 10^{10} per cm^3. For obtaining TL emission from a phosphorescent material, the material is first heated to the maximum temperature to clean all the electron-hole trapping levels and cooled to very low temperatures. The material is then excited/irradiated at this low temperature, at which the traps to be investigated do not lose their electrons/holes. The energy of excitation/irradiation should be larger than the energy gap of the material. After the material has been irradiated for a few minutes, it is heated with a uniform rate. The electrons/holes, which have been trapped during excitation start getting released involving radiative emission giving rise to TL. Thermal energy stimulates the carriers to cross the potential barriers of these traps and, in the process, allow them to move to the suitable recombination center that contains a hole or an electron resulting in the emission of light called TL. The pattern of luminescence output vs. temperature is called TL (or glow) curve.

When trapping levels are located at a fixed energy E_T below the CB (electron traps) or above the VB (hole traps) a single maximum exists in the glow curve. In case the traps are distributed in separate groups at different depths, the TL curve constitutes more than one maximum, such as the spectra shown in Figure 2.7. Each of these maxima represents a particular set of trapping levels. Knowing the temperature of maximum TL, the trap depth can be calculated. Since one can detect photons with high efficiency, TL, which is the result of excitation using ionizing radiation, can act as a sensitive technique for radiation dosimetry, an the TL intensity peak is directly related to the total radiation dose.
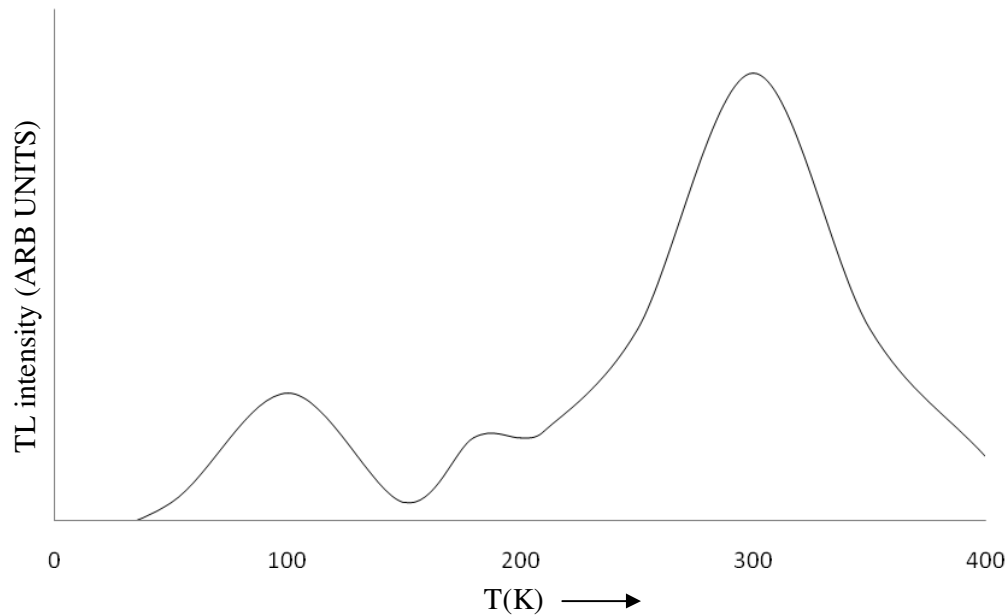
Figure 2.7 Schematic representation of a thermoluminescence curve

Electroluminescence: Electroluminescence (EL) is caused by excitation by an electric field. The emission characteristics of EL are similar to those observed in PL.

2.3. Phosphors and Theory of Phosphorescence

As mentioned previously, phosphors are materials, which convert radiation of one wavelength to radiation of another wavelength, the conversion being from a higher energy to a lower energy. They are widely used in, for example, fluorescent lamps (ultraviolet to visible), TV (electron impact to visible) and scintillators (X-Rays and γ-Rays to visible) [23, 25].

Phosphorescence is the emission of light from triplet-excited states, in which the electron in the excited orbital has the same spin orientation (*i.e.* parallel) as the ground-state electron. Transitions to the ground state are forbidden in such a situation. Fluorescence is the emission light from singlet-excited states, in which the electron in

the excited orbital has a spin of opposite sign (*i.e.* anti-parallel) to the second electron remaining in the ground-state orbital. Return to the ground state in this case is spin-allowed and occurs rapidly by the emission of a photon. Figure 2.8 shows the singlet and triplet spin states. The unpaired electrons of an excited molecule can either have their spins anti-parallel or parallel. The states with anti-parallel spins have spin quantum number $S = 0$ and are called singlets after their multiplicity. The states with parallel spins have $S = 1$ and are called triplets, and they tend to have lower energies than the singlets. The ground state is always a singlet.
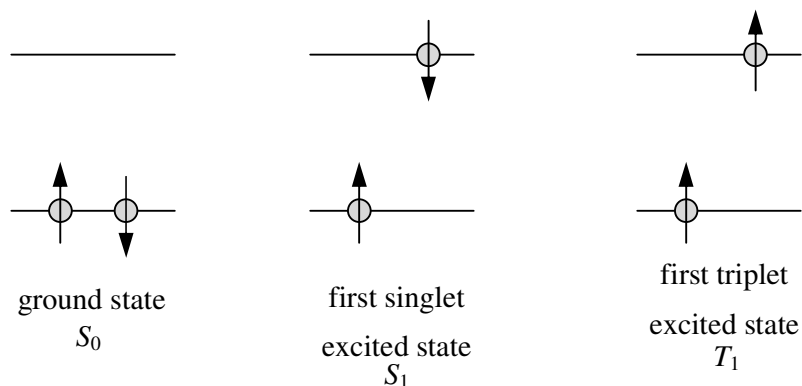
Figure 2.8 The possible spin states of a molecule

Processes taking place between the absorption and emission of light are usually shown on a Jablonski Diagram, which can be seen in Figure 2.9. In the diagram the electronic singlet states S_0, S_1 and S_2 along with three vibrational energy levels are shown. Here S_0 stands for the ground singlet state, and it represents the lowest vibrational level of the molecule. At room temperature, the higher vibrational energy levels are in general not populated (less than 1% according to Boltzmann statistics). The magnitude of the absorbed energy ($h\upsilon_A$ in Figure 2.9) decides which vibrational level of S_1 (or S_2) becomes populated. This process is very fast and occurs within 10^{-15} s. In the next 10^{-12} s the molecule relaxes to the lowest vibrational level of S_1, a process called internal conversion (IC). Since emission typically occurs after 10^{-9} s the molecule is fully relaxed at the time of emission. Hence, as a rule, emission occurs from the lowest vibrational level of S_1 (Kasha's rule), and the fluorescence spectrum is generally independent of the excitation wavelength. After emission ($h\upsilon_F$ in Figure 2.9) the molecule returns to the ground state, possibly after vibrational relaxation. This completes the simplest case of fluorescence: excitation, internal conversion, emission and relaxation. Apart from FL, phosphorescence may also take place. In order for this to

occur, after the excitation, when the electron is undergoing relaxation to the lowest possible vibrational level (S_1), intersystem crossing takes place and the spin state changes from a singlet (in this case S_1) to a triplet (T_1) that has a lower energy. This conversion would occur due to spin-orbit coupling. After such a nonradiative internal conversion, the triplet-to-ground state transition occurs, and this kind of emission is called phosphorescence [24].
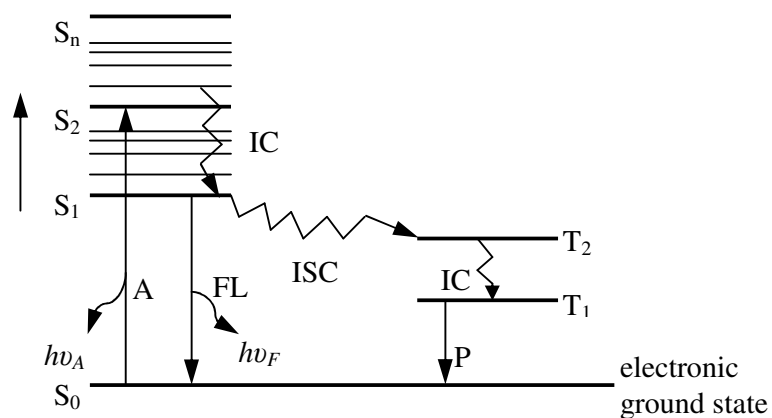
Figure 2.9 The Jablonski Diagram

As depicted in Figure 2.9, phosphorescence is generally shifted to longer wavelengths relative to FL. Transition from the T_1 to the singlet ground state is forbidden, and as a result, the rate constants for triplet emission are several orders of magnitude smaller than those of fluorescence. Also, the $T_1 \rightarrow S_0$ transition has a long radiative lifetime, because of the low transition probability.

For both fluorescence and phosphorescence, the Jablonski Diagram shows that absorption has a higher energy than the emission. This phenomenon is called a "Stokes shift" after George Gabriel Stokes who discovered this concept in 1852 [25].

2.4. Relating Structure to Optical Properties: Application of ELNES

In the study of solid-state samples, electron energy loss spectroscopy (EELS) in the transmission electron microscope (TEM) provides a valuable method of quantitative nanoscale chemical analysis that may be combined with the results of energy dispersive X-Ray (EDX) analysis to enable elemental determination at a high lateral resolution for many elements. .However, additional insight into the chemical and structural properties associated with the atom undergoing excitation may be gained via both qualitative and semi-quantitative analysis of the electron energy-loss near-edge structure (ELNES) associated with each core-loss ionization edge. In certain cases, analysis of the ELNES could allow the determination of two features of significant interest: the site symmetry of the nearest neighbor coordination atoms in complex structures and the valence state of the atom that is undergoing excitation. This approach facilitates the rapid identification of unknown phases in complex microstructures, the semi-quantitative determination of atom site occupancies, as well as the determination of local bonding at interfaces and defects using spatially resolved ELNES measurements. In order to develop a methodology for the use of such techniques, it is necessary to perform measurements on reference compounds with known structural and chemical properties. For example, clay minerals and clay-sized materials can be difficult to characterize by other analytical techniques because of they are heterogeneous at the nanoscale. Such materials could be characterized down to nanoscale by the help of ELNES [1].

Because ELNES is highly sensitive to the coordination symmetry of the ions present in the material, it was chosen specifically for this study on dopant effects on the electronic structure. In this thesis, ELNES is used as a tool to investigate firstly the homogeneity of the sample at the nanoscale. Moreover, since the ELNES could serve as a "fingerprint", whereby small perturbations in the crystal field around the ions is reflected on the spectrum, this technique is well suited for investigating the effects of the rare earth dopants that are subject of this study, Eu, Dy, in addition to the incorporation of boron. In this section, first the theory behind ELNES will be introduced

followed by some examples showing what could be achieved with ELNES, as it is was used in this study.

2.4.1. EELS vs. ELNES

Electron energy-loss spectrometry (EELS) in the transmission electron microscope (TEM) involves the measurement of the energy imparted to a thin ($\leq$ 200 nm) specimen via the scattering losses of fast ($\geq$ 100 keV) incident electrons. There are a number of ways in which the incident electrons interact with the specimen, giving rise to various features in the energy-loss spectrum. One of the most important of the possible energy-loss processes is atomic ionization, in which electrons are ejected from inner, or core, shells (*i.e.* the K-, L-, and M-shells, *etc.*) of atoms in the specimen. This process requires that the core electron undergoing excitation receives energy greater than or equal to the critical ionization energy, E_c, which is a function of the specific quantization energy level of the electron and is therefore uniquely defined for each atom and principal quantum number. That is, characteristic signals termed "ionization edges" appear in the spectrum at energy losses corresponding to E_c, thus identifying the presence of specific elements in the specimen. The edge intensity can be related directly and quantitatively to the amount of the element present. In addition to containing quantitative elemental information, the ionization edges have small intensity fluctuations, just above the edge onset, termed the energy-loss near-edge structure (ELNES). The ELNES has been found to be dependent on details of the local atomic environment such as coordination, valence and the type of the bonding. Measurement of such fine structure, understanding how it is related to the electronic structure and ultimately to materials properties can provide solutions to some previously unsolvable materials problem, where changes in bonding occur over small length scales. Thus, the main advantage of ELNES is the potential to examine changes in bonding with a spatial resolution at the nanometer lever and even approaching the level of interatomic spacings. In this way, not only could bonding in bulk materials be determined, but the changes in bonding at microscopic defects or nano-fabricated structures could also be examined [26,27].

During the ionization process, the inner-shell electrons are provided with sufficient energy to overcome the attraction of the nucleus and, if they do not escape

completely from the material, they are excited to empty available electronic energy levels (or states). These unoccupied energy levels are a function of the overall electron energy distribution based on the bonding interaction between the atom and its neighbors, *i.e.* the way in which the host atom is bonded to neighboring atoms in the crystal lattice. Thus, upon ionization, the atom itself is transformed from a ground state configuration into an excited state with an empty state (or hole) in the core shell and the ejected core electron in a previously unoccupied energy level (which may or may not be bound to the atom). The possible energies imparted to the ejected electron are controlled by the distribution (in energy) of these unfilled states. The distribution of the ground state energy levels plus that of the unoccupied levels thus constitute the joint density of states (JDOS). It is the dipole transition between the two sets of states that is mapped by EELS. Thus, fluctuations in intensity on the ionization edge, the ELNES, are directly related to the distribution of unfilled electron states and can be interpreted in terms of the bonding state of the ionized atom.

For the transition to be allowed, the change in the angular-momentum quantum number upon excitation (Δl) must be either -1 or +1. Thus, when considering the excitations from the $1s$ level or K shell ($l = 0$), the only significant transitions are to final states of p character ($l = 1$). L edges arise from transitions originating from the second atomic shell ($n = 2$). Transitions from the $2p$ level or $L_{2,3}$ shell ($l = 1$) accordingly involves transitions to both s- ($l = 0$) and d-character ($l = 2$) final states. The L shell also has an L_1 shell ($2s$ states, $l = 0$), which sits closer to the nucleus than the L_2 and L_3 shells, and its electrons can only be excited to a p state ($l = 1$), but not to a d state ($l = 2$), or to another s ($l = 0$) state. Table 2.1 shows the nomenclature and quantum numbers involved in the transitions for various EELS edges and Figure 2.10 is a schematic for the transitions [27].

20

Table 2.1 Nomencluture of the transitions that are taking place.

		Initial state quantum numbers			
Edge	Initial state	n	l	j	Final state symmetry
K	$1s^{1/2}$	1	0	1/2	p
L_1	$2s^{1/2}$	2	0	1/2	p
L_2	$2p^{1/2}$	2	1	1/2	s or d
L_3	$2p^{3/2}$	2	1	3/2	s or d
M_1	$3s^{1/2}$	3	0	1/2	p
M_2	$3p^{1/2}$	3	1	1/2	s or d
M_3	$3p^{3/2}$	3	1	3/2	s or d
M_4	$3d^{3/2}$	3	2	3/2	p or f
M_5	$3d^{5/2}$	3	2	5/2	p or f
N_1	$4s^{1/2}$	4	0	1/2	p
N_2	$4p^{1/2}$	4	1	1/2	s or d
N_3	$4p^{3/2}$	4	1	3/2	s or d
N_4	$4d^{3/2}$	4	2	3/2	p or f
N_5	$4d^{5/2}$	4	2	5/2	p or f
N_6	$4f^{5/2}$	4	3	5/2	d
N_7	$4f^{7/2}$	4	3	7/2	d
O_2	$5p^{1/2}$	5	1	1/2	s or d
O_3	$5p^{3/2}$	5	1	3/2	s or d
O_4	$5d^{3/2}$	5	2	3/2	p or f
O_5	$5d^{5/2}$	5	2	5/2	p or f
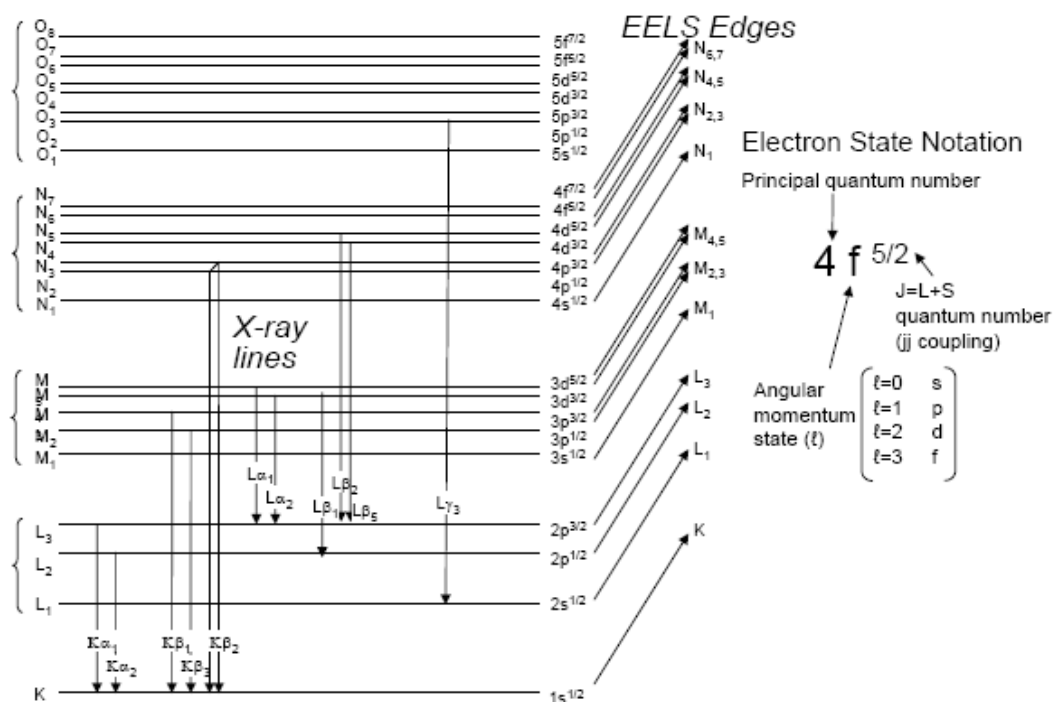
Figure 2.10 Schematic of the transitions happening.

A typical EELS spectrum that is seen in Figure 2.11 displays the electron intensity as a function of energy loss and can be divided into several regions. The large zero-loss peak (ZLP) results from transmitted electrons that have undergone elastic and quasi-elastic (mainly phonon) interactions, i.e., electrons that have undergone minimal energy. The region immediately following the ZLP and extending to energy losses of 50 eV, called the low-loss region, is an area of the spectrum dominated by plasmons. Plasmons can be described as resulting from the collective excitations of valence electrons. They can provide information about the dielectric function, valence electron densities, and in suitable cases, the phases present in alloys. Within the low-loss region are also found edges caused by transitions from outer shell electrons. Extending beyond the low-loss region in a spectrum from a thin sample is monotonically decreasing background, arising predominantly from plasmon and single electron excitations, on which are superimposed the core-loss edges. These features result from the interband transition of core electrons to unoccupied states. As mentioned above, this requires the energy transfer between the incident and a core electron to be greater than its binding energy [26,28].
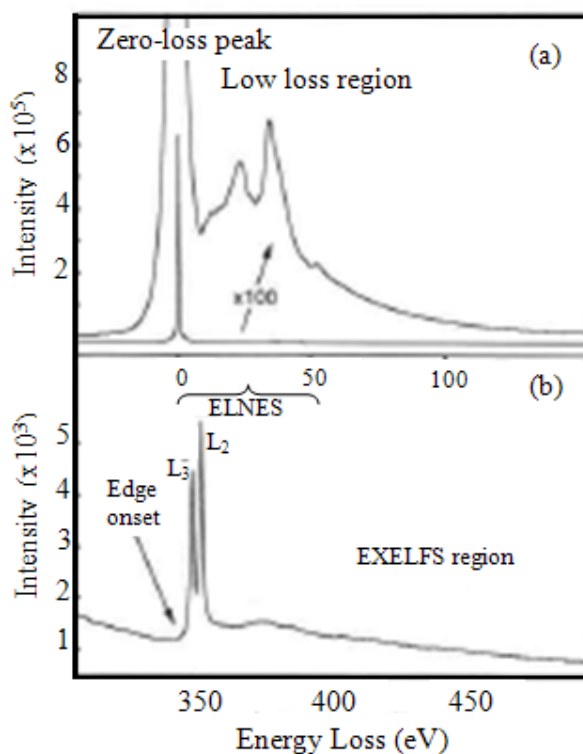
Figure 2.11 A representative EELS spectrum showing (a) the zero loss peak and low-loss region and (b) a core loss edge from the mineral gaudefroyite [26]

The core-loss edges usually take the form of a step, characterized by an abrupt increase in intensity that decreases with increasing energy loss. This feature can be seen in Figure 2.11.b. The sudden rise in intensity represents the ionization threshold, the energy of which approximately corresponds to the inner-shell binding energy and hence is characteristic of the element. Core-loss edges can be divided into two regions (Figure 2.11.b), the ELNES, extending 30-50 eV above the edge onset, and the weaker extended electron-energy loss fine structure (EXELFS). The ELNES directly probes the unoccupied orbitals and therefore reflects the environment surrounding the excited atom and can provide information on bonding, valency, coordination and site symmetry [26].

The basic ionization edges can be seen in Figure 2.12 [27].
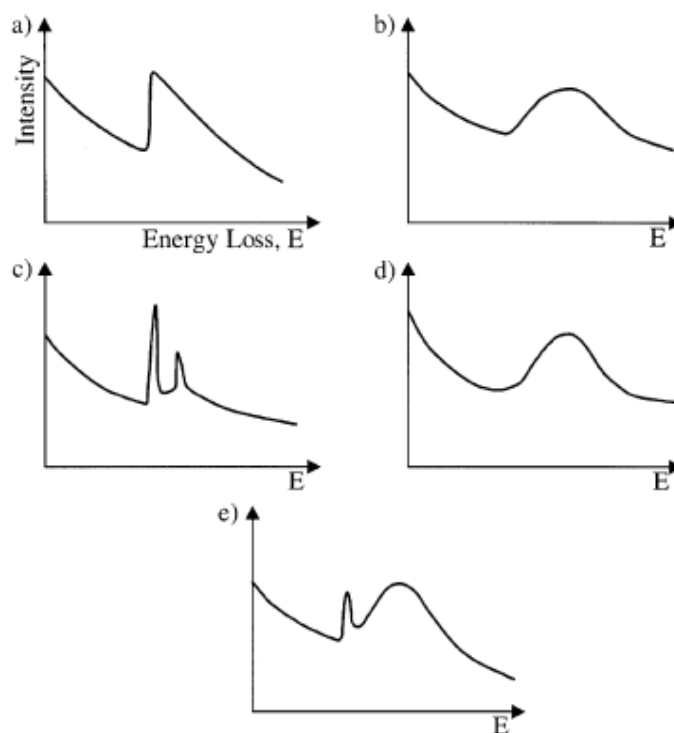
Figure 2.12 Schematic of the basic shapes of ionization edges. (a) Saw-tooth shape, e.g. K-edges. (b) Delayed maximum, *e.g.* characteristic of $L_{2,3}$-edges in 3rd period elements (Na to Cl), 4th period (Zn to Br) and $M_{4,5}$-edges for 5th period elements. (c) White lines, *e.g.* transition metals and rare earths. (d) Plasmon-like *e.g.* $M_{2,3}$ of 4th period elements (K to Ti). (e) Mixed, *e.g.* bound state plus delayed maximum.

An alternative way to interpret the ELNES fine structure is to imagine that the excess energy (greater than E_c) of the core electron is carried by a wave emanating from the ionized atom. If this wave has only a few eV of excess energy, it undergoes multiple elastic scattering from the surrounding atoms. Interference between the outgoing wave and the scattered waves is responsible for the ELNES. This can be envisaged as

analogous to a diffraction pattern, but with the θ scale replaced by an energy scale. If the outgoing wave has even more excess energy (typically more than 50 eV above E_c), then it is less likely to undergo multiple scattering, and we can approximate the interaction as a single-scattering event. Such higher-energy scattering produces very small-scale oscillations in the post-edge spectrum termed extended energy-loss fine structure (EXELFS), which contains information about the positions of neighboring atoms around the ionized atom. Both EXELFS and ELNES can thus be envisaged as a continuum of electron scattering, with the arbitrary distinction that ELNES is confined to a few tens of eV past the ionizations edge onset. While ELNES arises from a more complex process than EXELFS, it is more widely used, because the ELNES is a more intense and more easily measurable signal. In the low-loss EEL spectrum (< ~10 eV) transitions are measured from the valence band to the conduction band and can thus observe the band gap region directly. In ELNES, however, only the unoccupied states (the conduction band) are characterized, and many empty states within the band gap might be observed as a pre-edge intensity [27].

As mentioned previously, ELNES excitation involves transitions from a localized atomic inner shell to unoccupied final states near the core of the excited atom (*i.e.* final state whose wave functions have appreciable amplitude at a position corresponding to the atomic site undergoing excitation). The presence of the core hole also serves to contract the spatial extent of molecular orbitals and to localize the excitation even more as the outer states see a nucleus with an effectively greater positive charge.

ELNES could serve as a coordination fingerprint, because the general form of the ELNES is predominantly sensitive to the nearest neighbor coordination and hence the molecular orbital structure of the molecular unit present in the solid. The term "fingerprint" is used to emphasize that direct comparison with spectra from known standards is often all that is required for conclusive identification of the bonding state of a specific atom in the TEM specimen. Once the fingerprints are identified, then it is possible to fit these to the unknown spectrum, either directly or using a suitable algorithm, to determine semi-quantitatively, the proportions of various sites in a material. The lifetime of the core hole is much longer than the excitation process and so the outermost electron states, including the final state of the excitation process, would experience an attractive core hole potential. Generally, the core hole, an absence of an electron in an inner atomic level, behaves like an extra nuclear charge in the atom. This

extra positive charge may be shielded or screened by other electrons in the atom or solid (*e.g.* valence electrons), which could be re-distributed in response to the generation of the core hole and weaken its influence on outer lying electron states. However, overall this partially screened, positive, core hole potential would tend to bind outer electronic states more strongly, which would lead to a spatial contraction of the electron wave functions that are centered at the core hole site. This radial contraction would reduce the overlap of these excited-state wave functions with those wave functions centered on neighboring sites. Thus, the available final states in the presence of the core hole would (dependent on the degree of screening) become more sensitive to the short range environment of the excited atom. If an atom exists in two different environments in the lattice structure, then the ELNES is simply a linear superposition of the contributions from the two environments [27]. This site specificity has been demonstrated for solids containing atoms with a mixed coordination [29].

As an example of coordination fingerprinting, the basic features in the ELNES of MgO are determined primarily by the O sublattice and the cation arrangement simply adds some further fine features. In both MgO and $MgAl_2O_4$ the O sublattice has a FCC structure and so the O-K edges show very similar features which can be seen in Figure 2.13 [30].
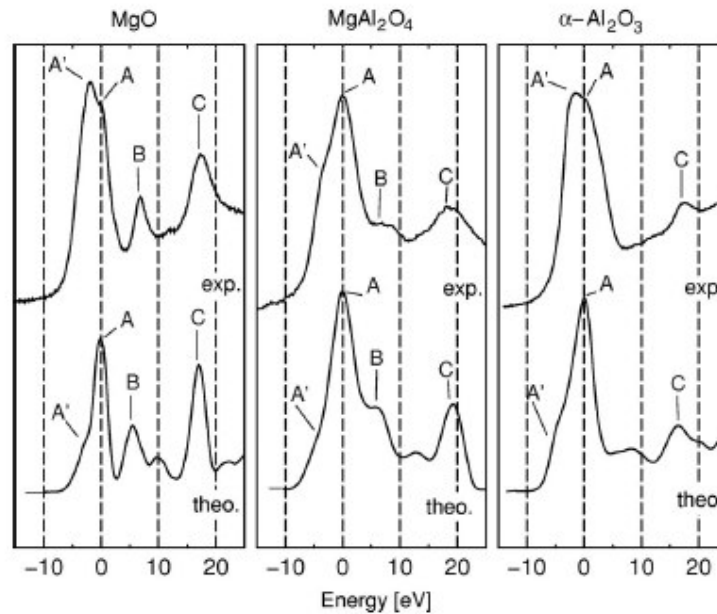
Figure 2.13 Comparison of the O-K edges for MgO, $MgAl_2O_4$ and alpha-Al_2O_3.

In their work, Gloter *et al* [29] have investigated the change in the O K-edge of the $Ca_2(Al_x, Fe_{1-x})_2O_5$ compound as x is varied between 0 to 67%. Looking at the changes, they have tried to understand the mechanism of bonding. Another group, Scheu *et al* in their work [31], aimed to determine the electronic structure and bonding of a $Cu\|\alpha$-Al_2O_3 interface grown by molecular beam epitaxy. This was approached by a comparison of the interfacial Cu $L_{2,3}$-, Al $L_{2,3}$- and O K-edge ELNES with measured standards.

In this present study, the need for using ELNES as a nanoscale characterization tool emerges from the fact that ELNES is very sensitive to changes in the crystal field. It is thus one of the most efficient ways to detect the structural perturbations of impurities and phase homogeneity. Phase homogeneity was an important factor in this study to model the electronic energy band diagram of the strontium aluminate compounds of interest. ELNES is also a useful tool in the quantitative detection of low weight elements ($Z < 4$), unlike EDX. Because we are interested in investigating the effects of boron, ELNES would be one of the few techniques suitable for analyzing the coordination changes, upon increasing the amount incorporated into the structure via changes in the B K-edges. The effect of dopants Eu and Dy could also be checked in terms of understanding the incorporation into the crystal structure, provided that the doping levels are above that sensible in ELNES. Also, the Al $L_{2,3}$-edges have been used to confirm the octahedral coordination of the Al cations.
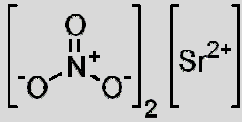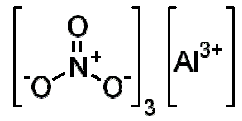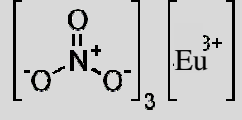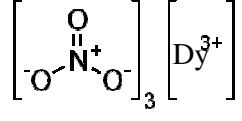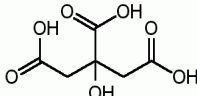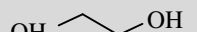
CHAPTER 3.   EXPERIMENTAL

In this chapter, the chemicals that were used during the experiments, the procedure as well as the characterization tools will be described. The procedure of both the original and the modified Pechini is given here. However, the discussion about the necessity of the modification of the original Pechini process is presented in Chapter 4.

3.1.   Chemicals

The chemicals that were used during the experiments are summarized in Table 3.1.

Table 3.1 Chemicals that were used for the experiments to obtain Strontium Aluminate Compounds

Name	Chemical Formula	MW (g/mol)	Supplier	Structure
Strontium nitrate anhydrous	$Sr(NO_3)_2$	211,63	Riedel de-Haer	
Aluminium nitrate nonahydrate	$Al(NO_3)_3.9H_2O$	375,13	Merck	
Europium (III) nitrate hexahydrate	$Eu(NO_3)_3.6H_2O$	446,07	Fluka	
Dysprosium (III) nitrate pentahydrate	$Dy(NO_3)_3.5H_2O$	438,59	Fluka	
Boron oxide	B_2O_3	69,62	Alfa Aesar	
Citric acid monohydrate	$C_6H_8O_7$	210,14	Merck	
Etyhlene glycol	$C_2H_6O_2$	62,07	Carlo Erba	

3.2. Procedure

In this section, the procedure of two different but similar experiments is given. The procedure of the original Pechini process, which is being used since 1960's, is presented before the modifications are explained in order to make a comparison between the two. The modified Pechini process is the base of this study and so it can be regarded as the main experimental procedure of this thesis.

3.2.1. Original Pechini Process

The basic Pechini process is relatively simple and versatile procedure that is widely used as a method for synthesizing ceramic systems. Under continuous stirring, the chelating agent, citric acid (CA), is added to boiling distilled water, followed by addition of the nitrate precursors ($Sr(NO_3)_2$, $Al_2(NO_3)_3.9H_2O$, $Eu(NO_3)_3.6H_2O$, $Dy(NO_3)_3.5H_2O$), according to the desired stoichiometric amount. When boron is added to the system, it is added as B_2O_3, and it is added to the distilled water after the nitrate precursors.

The citric acid amount is determined according to 1 mole of CA per mole of metal ion in the target composition, *e.g.* 5 moles for SA_2. After complete dissolution, heat treatment is performed in a box furnace at 250-300˚C to burn out the organics, dehydrate the solution and produce the amorphous precursor. A yellowish-orange smoke is observed, and as the last drops of the water is evaporated, a brownish yellow-colored foam is left, *i.e.* the amorphous precursor. In order to produce the crystalline strontium aluminate compound, the precursor is heated to temperatures between 700-1000˚C in an oxidizing environment. The strontium aluminate powders are obtained, after reduction at the same temperatures in a 96%N_2 and 4%H_2 forming gas environment.

3.2.2. Modified Pechini Process

Distilled water was taken into a beaker and was placed on a magnetic stirrer heater. The water was first boiled in order to get rid of the CO_2 that had dissolved in the water. The temperature of the distilled water was then reduced to and maintained at 80˚C. Strontium, aluminum, europium and dysprosium nitrate precursors were added to the water without a specific order according to the desired stoichiometric amounts, as listed in Table 3.2 to obtain 1 g of end–product.

Table 3.2 Amounts of the ingredients used in synthesizing $SrAl_4O_7$, $SrAl_{12}O_{19}$ and $SrAl_2O_4$ doped with 1mol%Eu, 1mol%Dy and 10mol%B

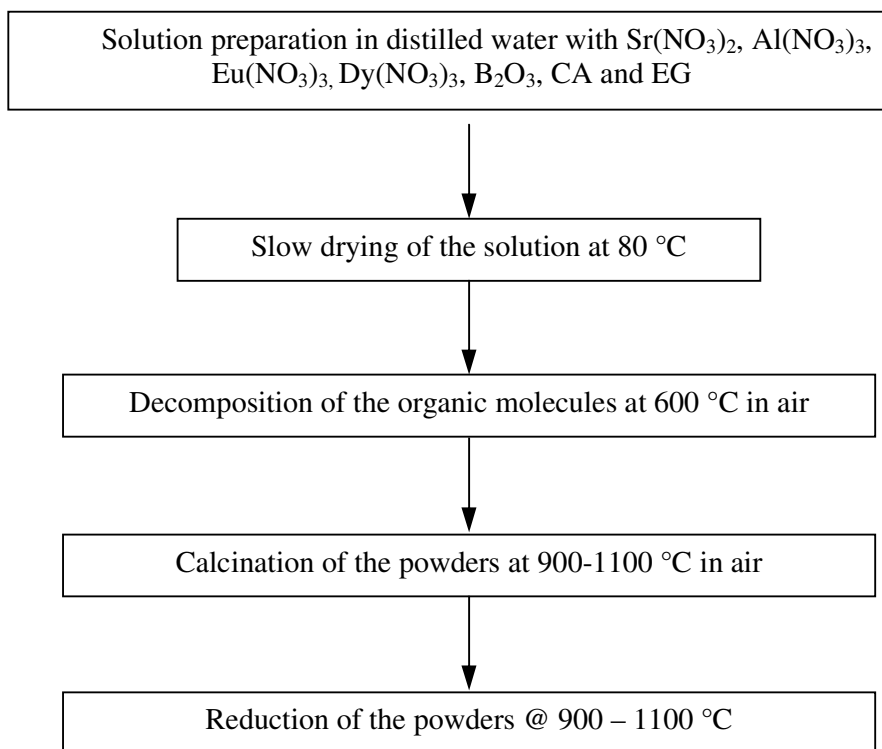| Ingredients	$SrAl_4O_7$	$SrAl_{12}O_{19}$	$SrAl_2O_4$
$Sr(NO_3)_2$	0,685032 g	0,295251 g	1,022500 g
$Al(NO_3)_3.9H_2O$	4,857135 g	6,280322 g	3,624955 g
$Eu(NO_3)_3.6H_2O$	0,014439 g	0,006223 g	0,021552 g
$Dy(NO_3)_3.5H_2O$	0,014197 g	0,006119 g	0,021191 g
B_2O_3	0,011267 g	0,004856 g	0,016818 g
CA	3,741163 g	4,192379 g	3,350506 g
EG	1,004558 g	1,125716 g	0,899660 g

B_2O_3 was added also to the solution. After complete dissolution, citric acid (CA) was added to the system, to achieve a 1:1 ratio of CA to total metal ions in the solution. Finally, the polyesterification agent, ethylene glycol (EG) was added, according to a 1:1 ratio of EG to CA. The solution was heat treated in a box furnace at 80˚C until all of the water had completely evaporated, leaving behind an amorphous precursor that was white in color. The amorphous precursor was then heat treated in a box furnace in an oxidizing environment, where it was heated to 600˚C with a 5˚C/min heating rate and held for 2.5 hours. The heating was then ramped at a rate of 5 ℃/min. to 900-1100˚C, with the precise temperature determined by the desired final strontium aluminate compound. Complete oxidation was determined to require 5 hours at the target treatment temperature.
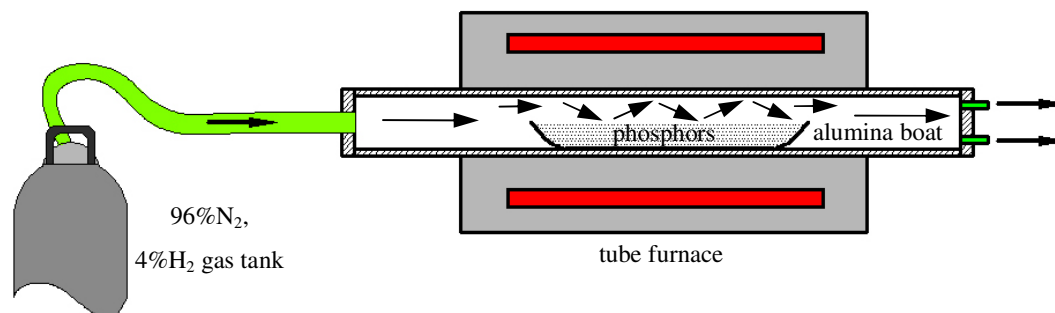
Figure 3.1 Schematic of the tube furnace used during the reduction process

```
┌─────────────────────────────────────────────────────────────┐
│  Solution preparation in distilled water with Sr(NO₃)₂, Al(NO₃)₃, │
│  Eu(NO₃)₃, Dy(NO₃)₃, B₂O₃, CA and EG                         │
└─────────────────────────────────────────────────────────────┘
                              │
                              ▼
┌─────────────────────────────────────────────────────────────┐
│            Slow drying of the solution at 80 °C              │
└─────────────────────────────────────────────────────────────┘
                              │
                              ▼
┌─────────────────────────────────────────────────────────────┐
│   Decomposition of the organic molecules at 600 °C in air   │
└─────────────────────────────────────────────────────────────┘
                              │
                              ▼
┌─────────────────────────────────────────────────────────────┐
│     Calcination of the powders at 900-1100 °C in air        │
└─────────────────────────────────────────────────────────────┘
                              │
                              ▼
┌─────────────────────────────────────────────────────────────┐
│         Reduction of the powders @ 900 – 1100 °C            │
└─────────────────────────────────────────────────────────────┘
```

Figure 3.2 Flow chart of synthesizing strontium aluminate compounds

Afterwards, the furnace was slowly cooled to room temperature, and the powders were placed in an open alumina boat and reduced for 3 hours in a tube furnace in a forming gas (96%N_2, 4%H_2) atmosphere, at the same temperature as the oxidation stage. The schematic of the heating at the tube furnace is seen in Figure 3.1, whereas the flow chart of the procedure described above may be found in Figure 3.2.

Various strontium aluminate compounds were synthesized via the mentioned experimental procedure. These are shown in Table 3.3.

Table 3.3 Various strontium aluminate compounds were synthesized with the modified Pechini process

	Pure	Eu mole%				Dy mole%				B mole%				
		0.3	0.6	1	5	0.3	0.6	1	5	1	5	10	20	30
SA₂	✓	✓	✓	✓	✓	✓	✓	✓		✓	✓	✓	✓	✓
SA₆	✓			✓	✓			✓	✓					

This procedure resembled Tang *et al.*'s sol-gel method, which yielded multiphase SA compounds [12]. However, in the end, we had succeeded in synthesizing highly crystalline and single-phase strontium aluminate compounds with this method.

3.3. Characterization Tools

To characterize the phase and chemical composition of the powders produced, as well as the optical properties, a variety of spectroscopy techniques were used. X-ray diffraction (XRD) (Bruker AXS Advance D8) with a Cu-K$_\alpha$ source revealed the initial details of phase purity and composition. However, the structural sensitivity limits were reached and higher spatial resolution was required. To this end, electron energy loss spectroscopy (EELS), energy loss near edge spectroscopy (ELNES), energy dispersive x-ray spectroscopy (EDS) measurements using a Vacuum Generators VG HB501UX dedicated scanning transmission electron microscope (STEM) operated in UHV at an accelerating voltage of 100 kV. This microscope has a cold field emission source and is equipped with an energy-dispersive X-ray spectrometer (Thermo Fischer Scientific, Noran System SIX) and an electron energy-loss spectrometer (Gatan UHV Enfina system). Finally, optical properties were also characterized by photoluminescence and phosphorescence spectroscopy using a HeCd laser (λ_{ex} = 325nm, KIMMON) and a fluorescence-specific spectrometer (Ocean Optics USB2000-FLG) , while cathodoluminescence imaging enabled spatial and topographical correlation with phase and the corresponding optical properties, using a field emission scanning electron microscope (SEM) (Leo Supra 35VP).

CHAPTER 4.   RESULTS AND DISCUSSIONS

In order to investigate the relationship between processing, composition and phase stability, first two target strontium aluminate phases were chosen for study, SA_2 and SA_6. The ceramic powder processing that is described in the previous chapter is a modification of the relatively low-temperature Pechini method, in which the processing steps were adjusted to enable better control over the production of single phase compounds. Next, with the suitable processing procedure, the impact of dopant composition on the overall phase stability was investigated by varying the Eu^{2+} dopant concentration: 0, 0.33, 0.66, 1, and 5 mol%. Finally, we looked into the effect of boron concentration on the overall phase stability of the Eu and Dy co-doped phases. In this chapter, first, the necessity of the modification of the original Pechini process for strontium aluminate compounds is discussed. In addition, the results of the original and the modified Pechini process are presented with discussions.

4.1.   Pure Strontium Aluminate Compounds

The first set of results is obtained with the powder X-Ray diffraction analysis (XRD) of the powders produced by the original Pechini method. These results revealed a mixture of different phases of strontium aluminates in a single sample, in addition to $SrCO_3$. Figure 4.1 shows a typical spectrum from these powders, where the target

compound is pure SA_2. The red lines show the JCPDS card peaks for the SA_2 compound. However, there were also peaks in the sample that did not match with the card lines, suggesting that the specimen did not consist of only a single phase of the SA_2 compound.
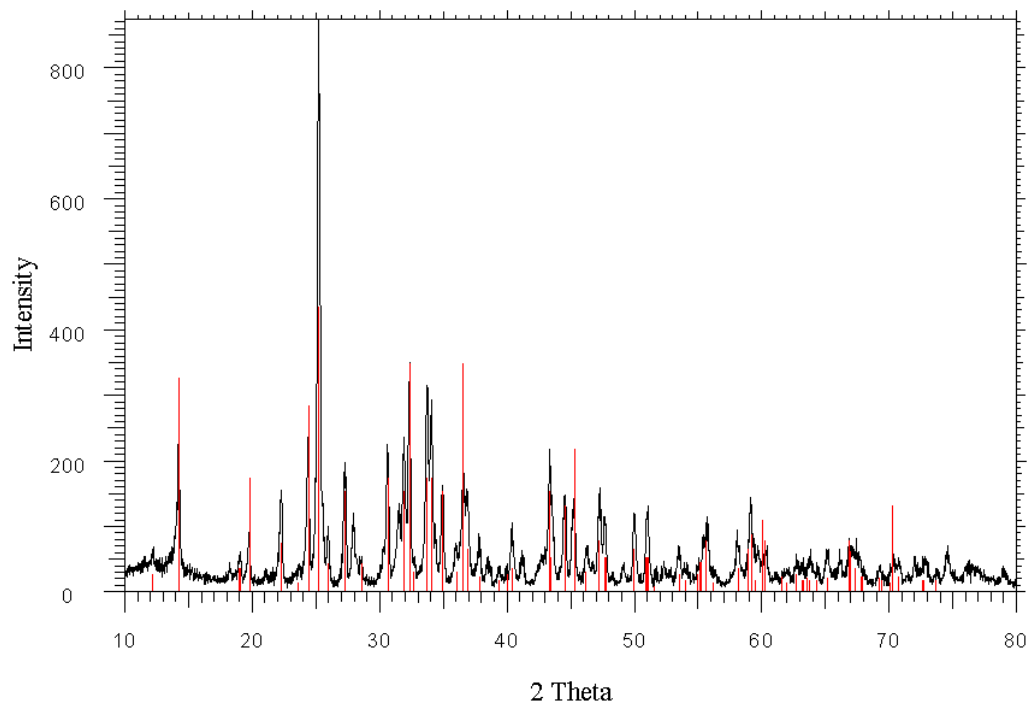

Figure 4.1 XRD of the SA_2 powders obtained via the original Pechini process. JCPDS card 25-1208 for SA_2 is indicated by the vertical red lines.

Preliminary studies were performed to characterize the electron density distribution of the ions, *i.e.* the crystal field, in the crystal lattice by Energy Loss Near Edge Strusctures (ELNES) with scanning transmission electron microscope (STEM). The Al $L_{2,3}$-edge ELNES spectra shown in Figure 4.2 were collected from measurements of 3 different regions of the same sample, indicating that the sample were not single-phase. The fact that the samples did not consist of single phase was concluded from the changes in the characteristic edges observed. These results demonstrated that single-phase compounds were necessary for this study, because our goal was to construct a model for the electronic structure, in order to understand the mechanisms of phosphorescence persistence. Any variation in the lattice parameters due to multiple phases would introduce ambiguity in the relative positions of the allowed electronic energy levels, and consequently in the excitation and emission wavelengths

that are referenced to either the bottom of the conduction band or the top of the valence band. Moreover, the electron density around each ion is strongly influenced by the neighboring lattice ions, via both the coordination number and the bond strength. Minimizing variations in the electron density stemming from different ionic configurations in different phases would decrease the variation in ELNES spectra (see Figure 4.2), and enable elucidation of the nature of the electron traps as determined by ion interaction.
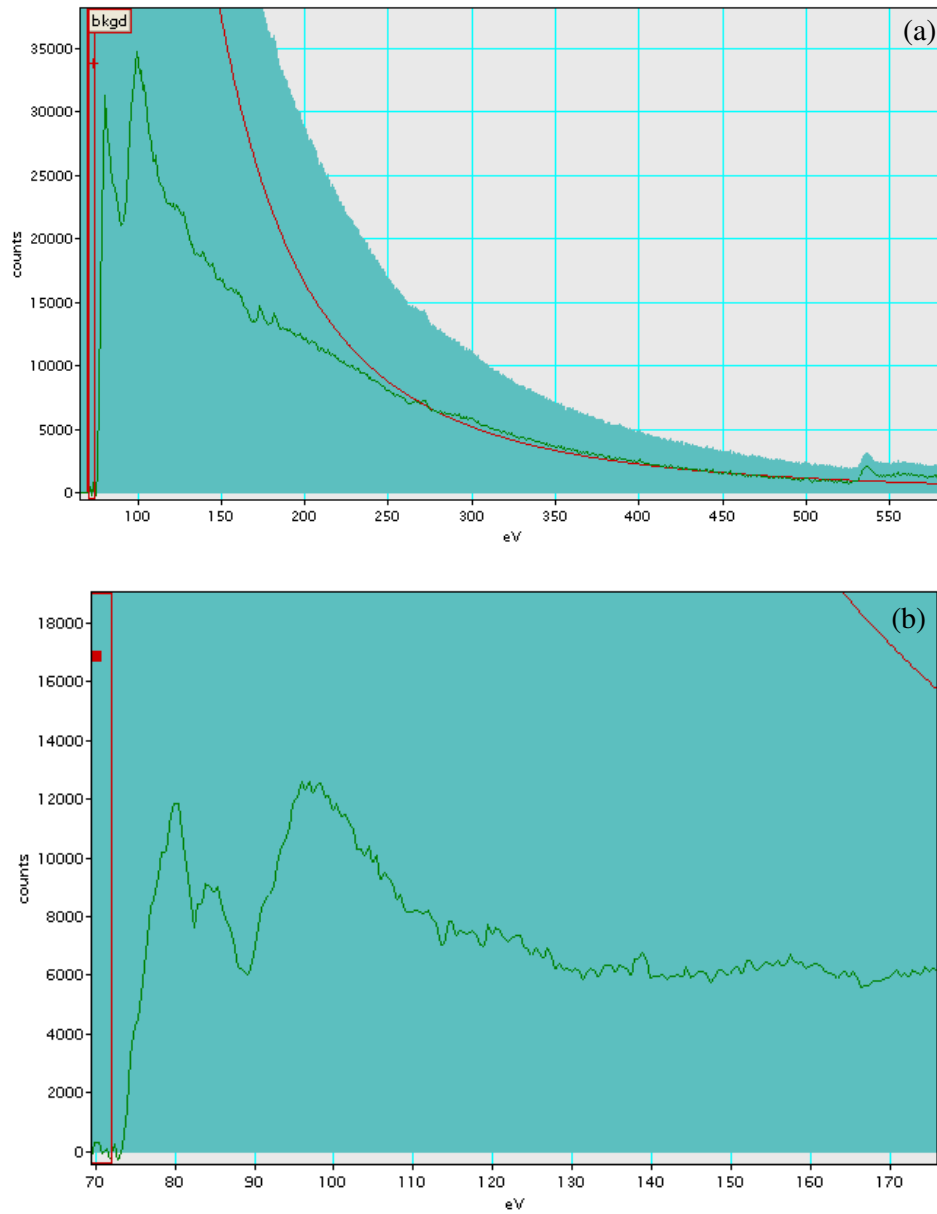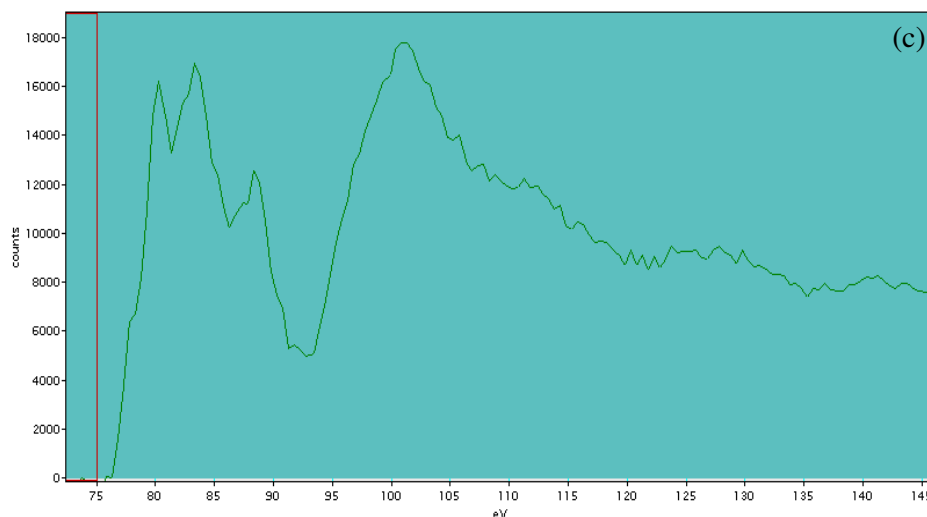
Figure 4.2 Variation in types of crystal structure in the same sample is apparent in the near-edge features of the ELNES spectra measured from 3 different particles.

Several attempts were made to eliminate the $SrCO_3$, which was thought to be the main problem leading to other phases. It appeared that during the removal of the organic components at temperatures around 250°C, CO_2 formed as a result of some combustion reactions. Sr^{2+} cations, which have a high affinity towards CO_3, had reacted with the dissolved CO_2 in the aqueous solution and as a result, precipitated as $SrCO_3$. This precipitation changed the stoichiometry of the ingredients during crystallization.

Thus, it is important to prevent the premature combustion of the precursor. To solve this problem, the Pechini process was modified, such that the water was evaporated while avoiding organic burnout, as described in Section 3.2.2 above. With the addition of the ethylene glycol (EG) as a polyesterification agent, the process yielded highly crystalline and single phase strontium aluminates doped with Eu and Dy.

4.2. Dopant Added Strontium Aluminate Compounds

In this section, the results are presented for the doping the strontium aluminate compounds with Eu, Dy, and B.

4.2.1. SA$_2$ Doped With Eu

After the successful synthesis of the single phase, crystalline compounds of SA$_2$ verified by the XRD, the effect of rare-earth dopant concentration on the atomic and electronic structure of SA$_2$ was studied by varying the Eu^{2+} concentration;0.33, 0.66, 1, and 5 mol%. The ELNES were inspected by STEM, which also showed that the crystal field around the ions had not changed significantly upon the addition of Eu^{2+}, but only up to 1 mol%, above which the Eu$_2$O$_3$ phase was also observed. In an attempt to study the differences in the ELNES spectra, low concentrations of Eu dopant were investigated: 0.33 mol% Eu and 0.67 mol% Eu. Figure 4.3 shows the corresponding bright field and high angle annular dark field images of the 0.33 mol% Eu-doped SA$_2$.

In general, according to the 27 different measurements performed on both the 0.33 mol% Eu and the 0.67 mol% Eu samples, Figure 4.4 and Figure 4.5 show that the Al L$_{2,3}$-Edge and O K-Edges remained consistently the same. Because this was the case within the same sample as well as between samples of different doping amounts, these results suggested that the samples had maintained the phase purity, in spite of the dopants. This also suggests that the europium atoms have been incorporated into the crystal structure of the SA$_2$, and the crystal field around oxygen and aluminum has not changed. However, it is also possible that these low concentrations were below the sensitivity level of the VG STEM.

Figure 4.4 is showing the Al L$_{2,3}$ edge ELNES for the 0.33 mol% Eu-doped SA$_2$ samples. The three different results are presented here, and they belong to different parts of the sample as indicated in Figure 4.3.
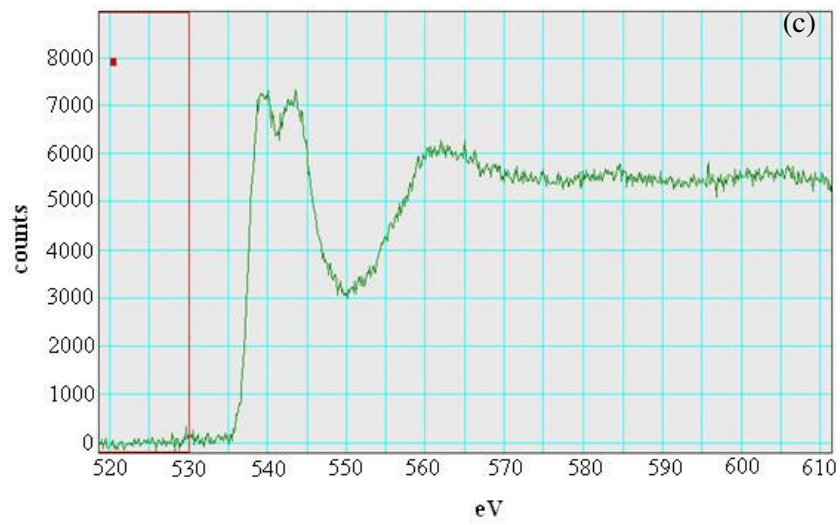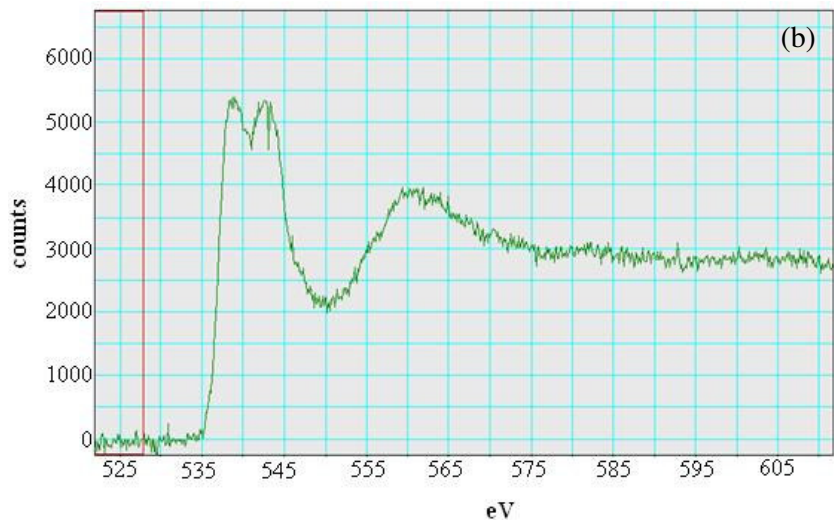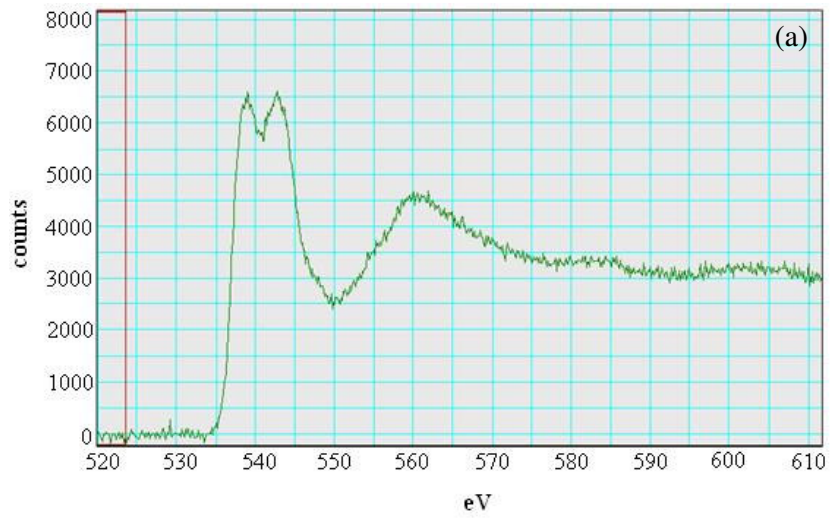
Figure 4.5 is showing the O-K edge ELNES for the 0.33 mol% Eu-doped SA$_2$ samples and again, the results correspond to different parts of the powders.
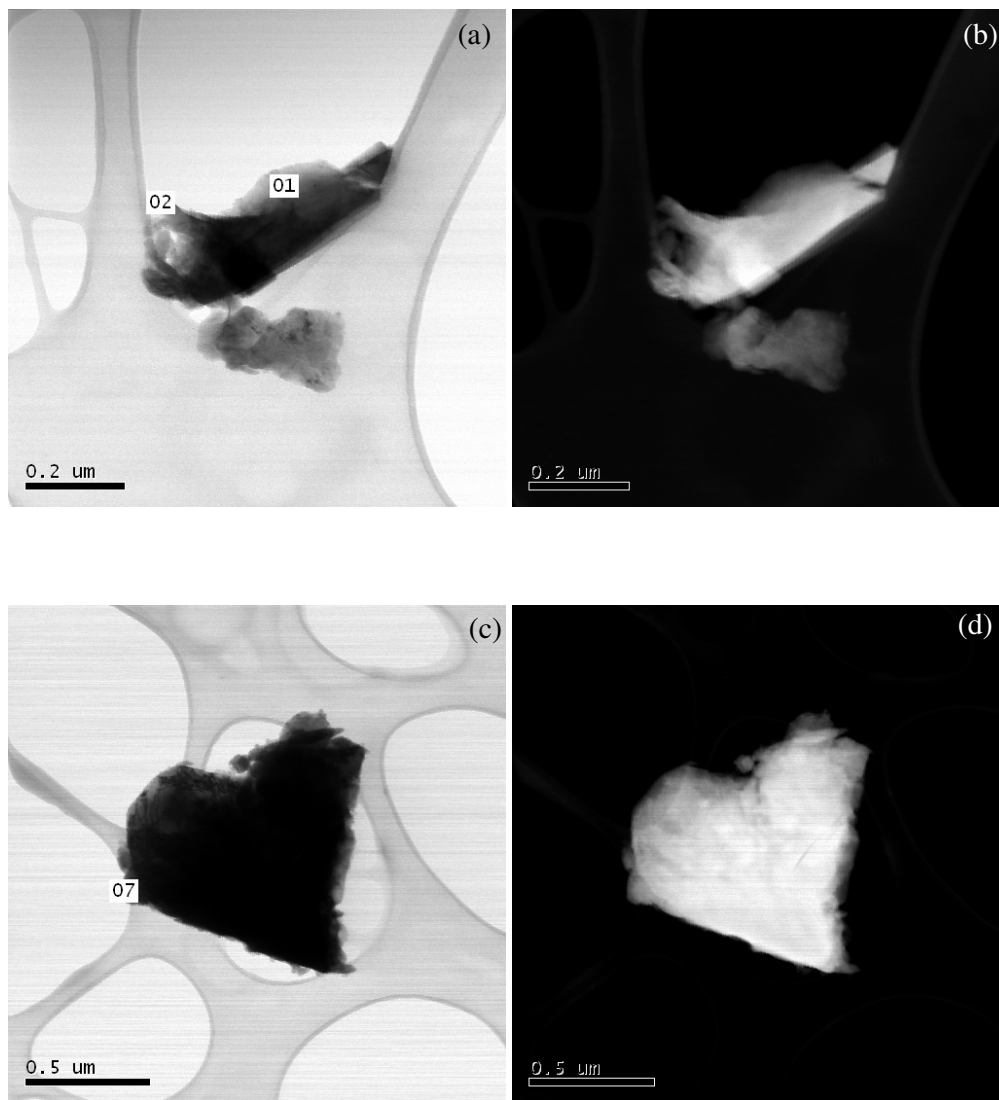
Figure 4.3 (a) and (c) Bright field image, (b) and (d) high angle annular dark field image of 0.33 mol% Eu-doped SA$_2$ as observed in the D-STEM
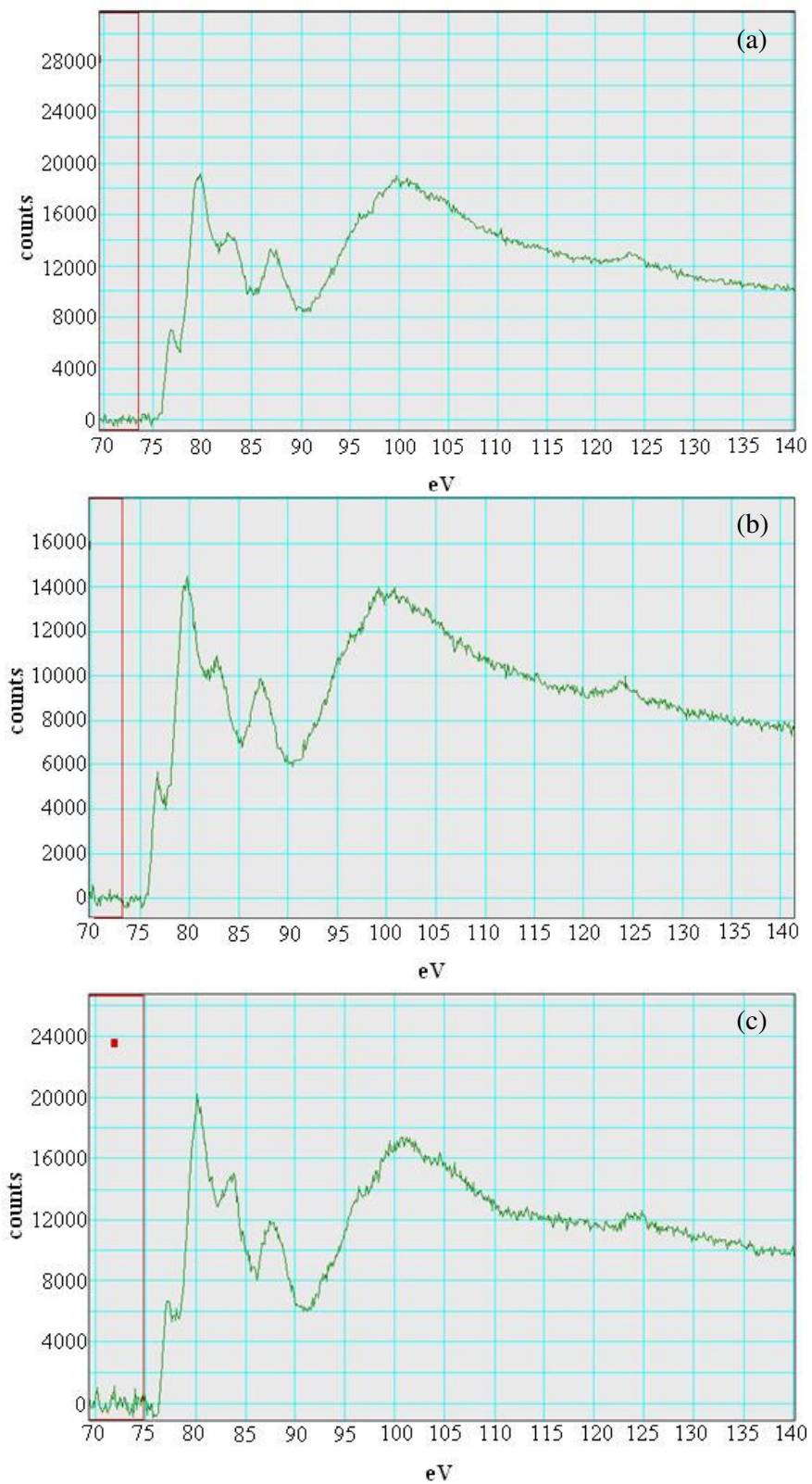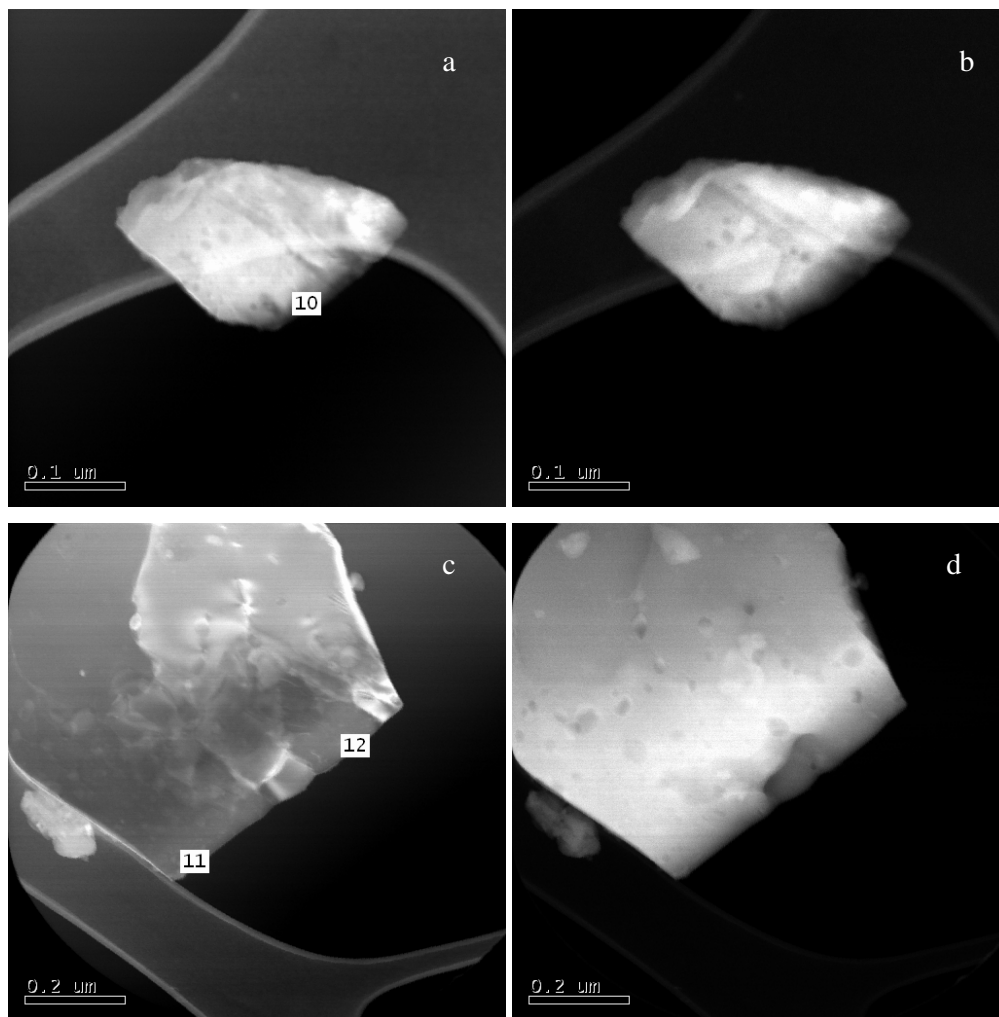
Figure 4.4 Al $L_{2,3}$-Edge ELNES structure of 0.33 mol%Eu-doped SA_2 measured from the (a) 01 point of the Figure 4.3.a (b) 02 point of the Figure 4.3.a (c) 07 point of the Figure 4.3.c
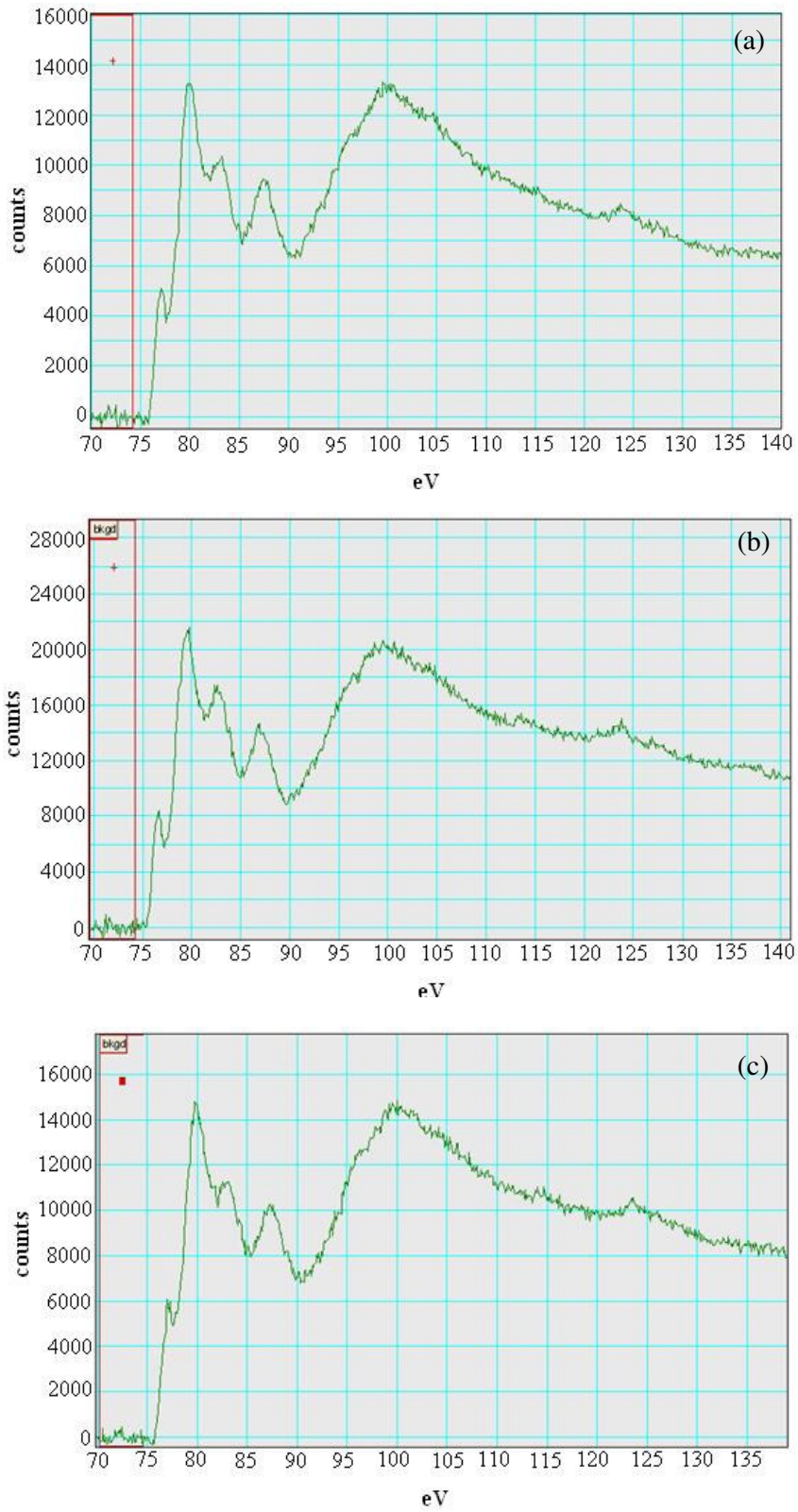
Figure 4.5 O K-Edge ELNES structure of 0.33 mol% Eu-doped SA_2 measured from the (a) 01 point of the Figure 4.3.a (b) 02 point of the Figure 4.3.a (c) 07 point of the Figure 4.3.c

Figure 4.7 is showing the Al L$_{2,3}$ edge ELNES for the 0.67 mol% Eu-doped SA$_2$ samples. The three different results that are presented here belong to different locations of the samples as indicated in Figure 4.6. Similarly, Figure 4.8 is showing the O-K edge ELNES for the 0.67 mol% Eu-doped SA$_2$ samples taken from the same locations shown in Figure 4.6.
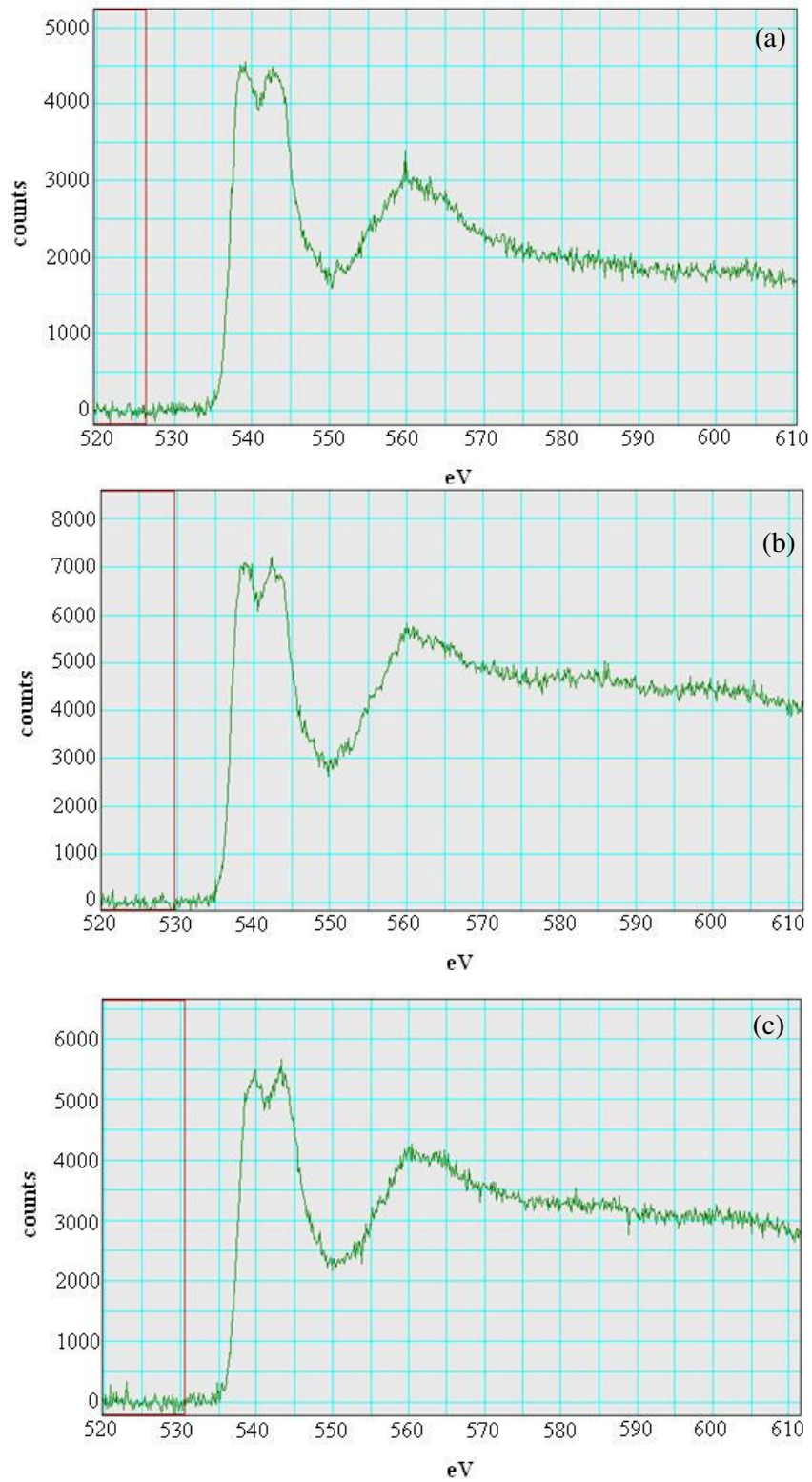

Figure 4.6 (a) and (c) Bright field image, (b) and (d) high angle annular dark field image of 0.67 mol% Eu-doped SA$_2$ as observed in the D-STEM

Figure 4.7 Al L$_{2,3}$-Edge ELNES structure of 0.67 mol% Eu-doped SA$_2$ measured from the (a) 10 point of the Figure 4.6.a (b) 11 point of the Figure 4.6.c (c) 12 point of the Figure 4.6.c

Figure 4.8 O K-Edge ELNES structure of 0.67 mol% Eu-doped SA_2 measured from the (a) 10 point of the Figure 4.6.a (b) 11 point of the Figure 4.6.c (c) 12 point of the Figure 4.6.c

4.2.2. SA₂ Doped With Eu and Dy

The effect of rare-earth dopant concentration on the atomic and electronic structure of SA_2 was studied by varying both the Eu^{2+} and Dy^{2+} concentrations: 0.33, 0.66, and 1 mol%. The powders produced by the modified Pechini process with a 1 mol% Eu^{2+} doping concentration had remained single-phase and with a high degree of crystallinity, as evidenced by the XRD spectra in Figure 4.9 for SA_2 doped with 1 mol% Eu and 1 mol% Dy. Figure 4.9 shows that all the peaks of the JCPDS card of SA_2 are well-matched for both the reduced and unreduced powders.
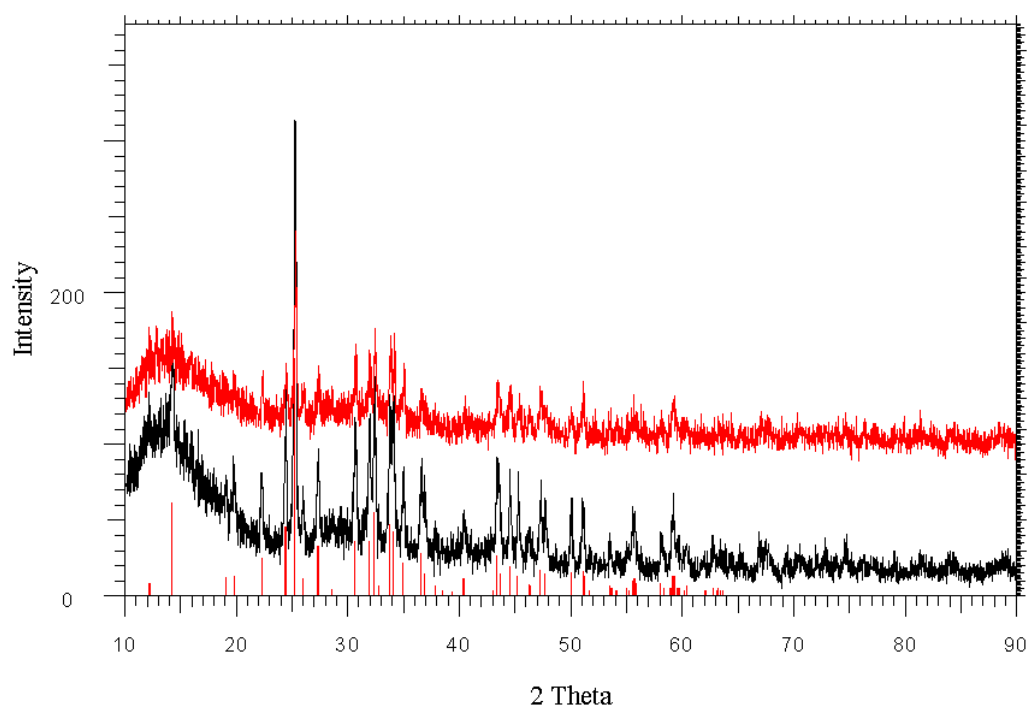

Figure 4.9 XRD of reduced *vs* not-reduced SA₂:1%Eu, 1%Dy powders that are obtained by the modified Pechini process. The red rod-like lines correspond to the JCPDS card 25-1208. (a) calcinated, unreduced powders (b) reduced powders.

The crystallinity can be seen in the SEM images presented in Figure 4.10. Visually, one can observe that, the secondary electron SEM images of the 1 mol% Eu, 1 mol% Dy-doped amorphous SA_2 show smooth and circular edges (see Figure 4.10.a), while the images that are taken after the calcination and reduction processes show sharper edges (see Figure 4.10.b). Also, it can be seen that the particle sizes of the powders are around 5-10 µm.
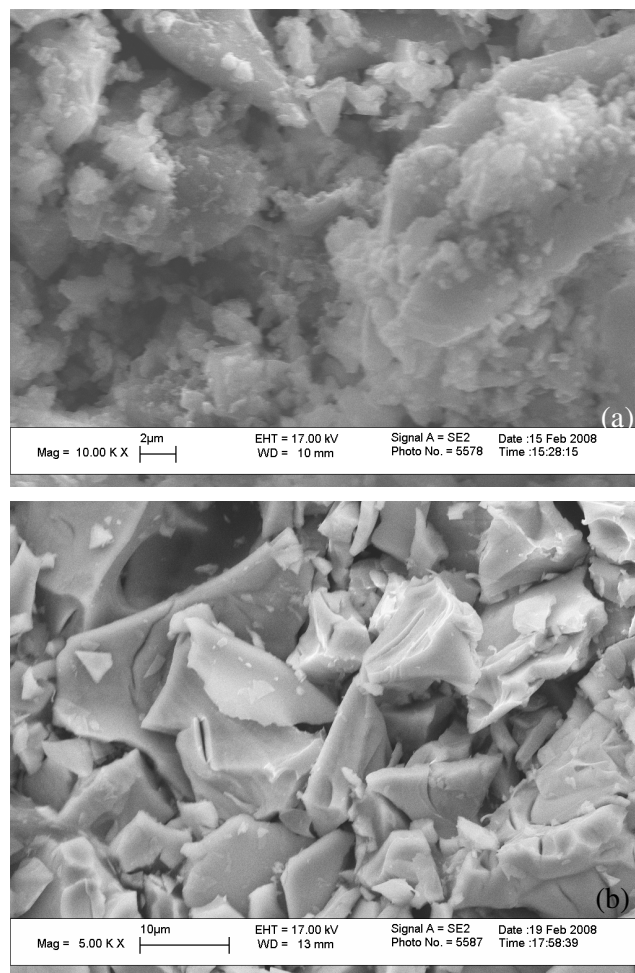
Figure 4.10 Secondary electron SEM images of 1%Eu, 1%Dy doped SA$_2$ (a) amorphous (b) after calcination and reduction.
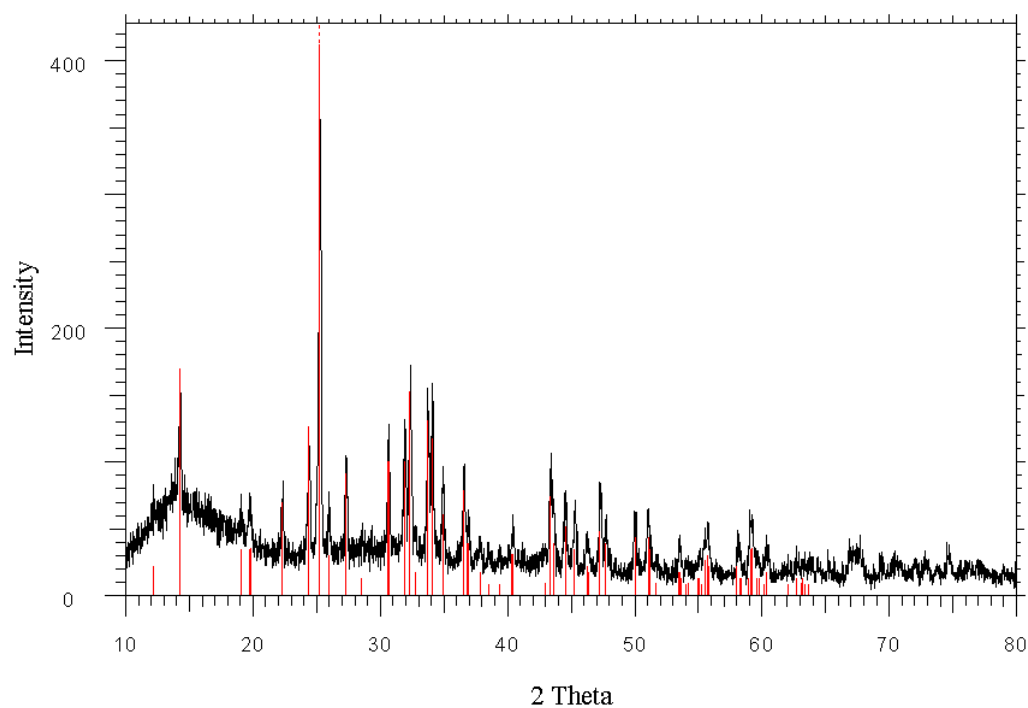
A typical EELS spectrum of the 1 mol% Eu and 1 mol% Dy doped SA$_2$ powders might be found in Figure 4.11. It can be seen that the band gap of this sample corresponds to 6-6.5 eV which is in agreement with literature [9].
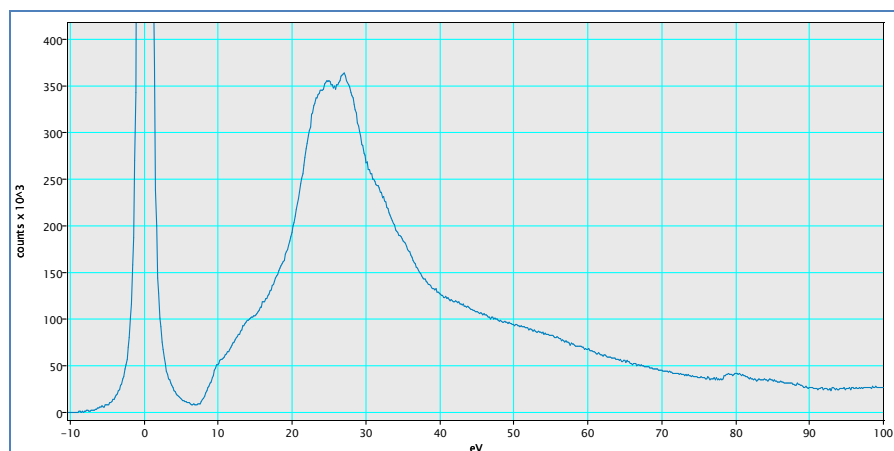
Figure 4.11 EELS spectrum of 1 mol% Eu, 1 mol% Dy doped SA_2

4.2.3. SA_2 Doped With Eu, Dy and B:

Figure 4.12 shows the XRD spectra of the 1 mol% Eu, 1 mol% Dy and 10 mol% B-doped SA_2.
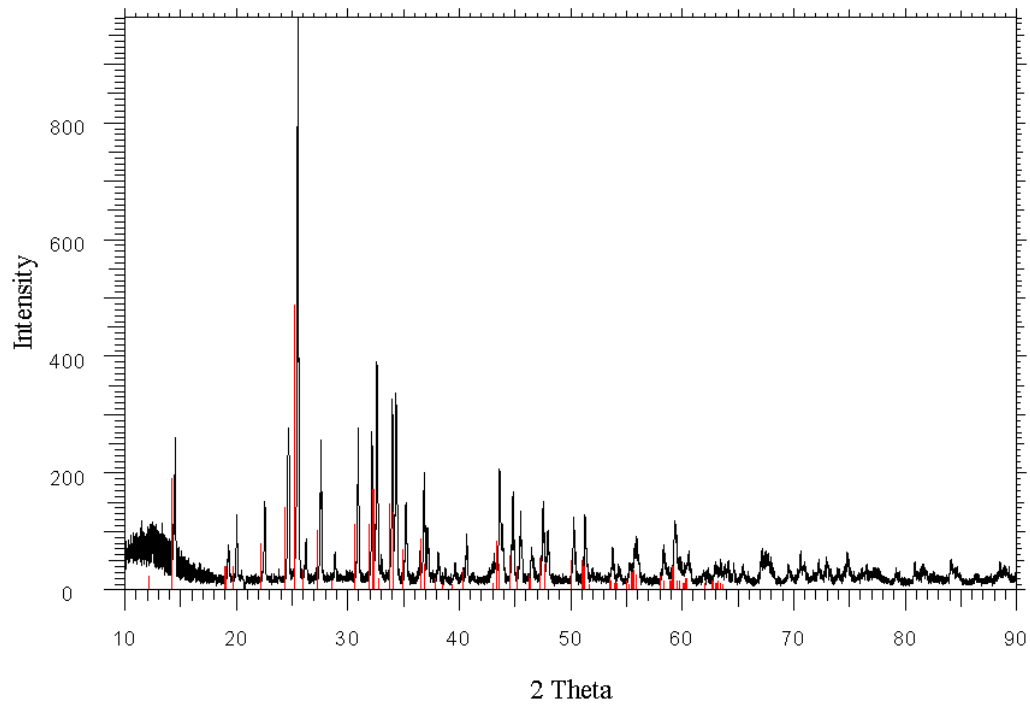

Figure 4.12 XRD results of SA_2:1%Eu, 1%Dy, and 10% B showing high crystallinity. The red vertical lines represent the JCPDS card #25-1208.

Compared with those in Figure 4.10, it can be seen that the crystallinity of SA_2 has increased with the addition of B. This was an expected result. Since boron is used as a flux in the solid-state reaction synthesis, it has been reported before that addition of boron to the system enhances the crystallinity.

However, comparing the XRD of 10 mol% B-doped samples with those of 20 mol% B (see Figure 4.13) and 30 mol% B (see Figure 4.14), it is seen that the crystallinity is further enhanced for increasing amounts of boron in the system. This is an interesting result that contradicts with what has been reported previously in the literature. To date, it has not been possible to dope the material with 30 mol% B, without disturbing the crystal lattice and introducing some amorphous phase to the system. Usually, it is believed that since boron is much smaller than aluminum, there is a certain amount that boron can replace aluminum in the structure. Thus, solid solutions could be expected only up to a certain limit. It was observed before that, after 20 mol% boron content, the amorphous regions appeared at around 20-40° 2θ [9]. However, with our proposed method, it is possible to incorporate 30 mol% B into the material without introducing any amorphous phase to the structure. This might be due to the fact that with our method, when the solution of ions is formed, the cations are distributed homogeneously in the distilled water, and this might be the reason for easier diffusion during calcination.

Another consequence of increasing the boron content in the material is that, as the boron amount is increased, not only the crystallinity increases, but also there is a shift in the diffraction angles (2θ). This can be understood better via Figure 4.15, in which the 10, 20 and 30 mol% B doped SA_2:1 mol% Eu, 1 mol% Dy results are being compared.

Figure 4.13 XRD results of SA$_2$:1%Eu, 1%Dy, and 20% B showing high crystallinity. The red vertical lines represent the JCPDS card 25-1208.
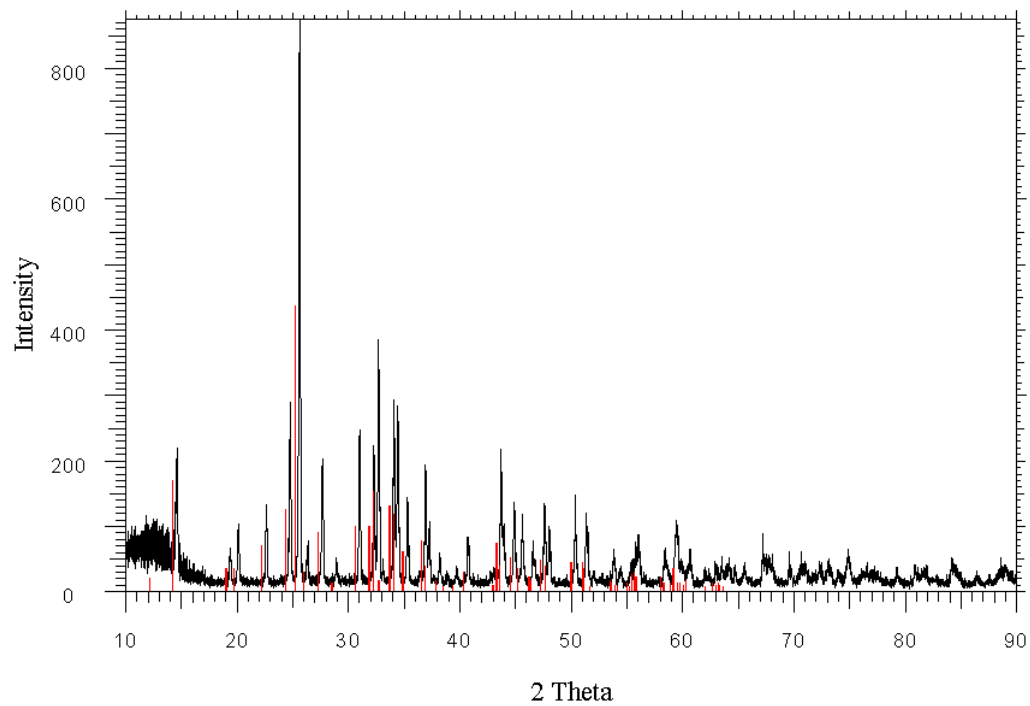
Figure 4.14 XRD results of SA$_2$:1%Eu, 1%Dy, and 30% B showing high crystallinity. The red vertical lines represent the JCPDS card #25-1208.

As it can be seen in Figure 4.15, the boron content in the material had increased from 10 to 20 and then to 30 mol%, while the 2θ values are increasing from 25.22 to 25.49 and then to 25.58°.
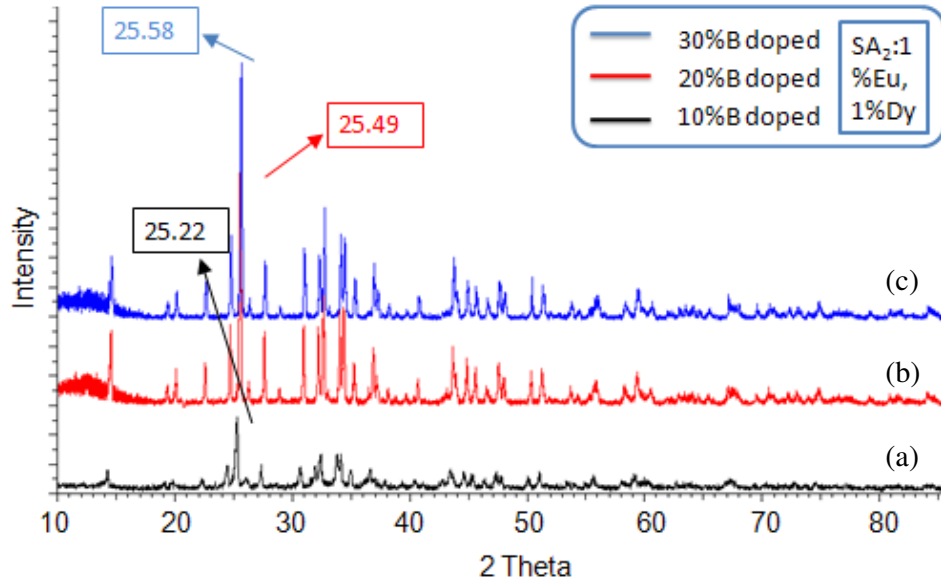
Figure 4.15 Comparison of the (a) 10%, (b) 20%, (c) 30% B doped SA$_2$:1%Eu,1%Dy

According to Bragg's Law, the diffraction angle in the material is related to the *d*-spacing in the materials and hence, the lattice parameter with the relation:

$$n\lambda = 2d\sin\theta \tag{3.1}$$

and *d* is related to the lattice parameter *a* with the relation:

$$d = \frac{a}{\sqrt{(h^2 + k^2 + l^2)}} \tag{3.2}$$

Thus, as *θ* increases, sin*θ* increases as well. Since the wavelength of the x-ray source is fixed, then as sin*θ* increases, *d* has to decrease. Smaller d means that the lattice parameter gets smaller as well. The conclusion is that, the crystal lattice shrank with increasing boron content. Since XRD spectra did not show any amorphous features, this suggests that boron had been incorporated into the crystal lattice substitutionally, rather than interstitially. Moreover, since the crystal size shrank, one possible conclusion is that, since boron is much smaller than aluminum, it may have substituted onto an Al lattice site. Another conclusion is that, if boron entered the crystal lattice as an interstitial, than the result would probably be an increase in the crystal lattice size rather

49

than shrinkage upon incorporation of 30% B. According to the XRD spectra, however, this does not seem probable.
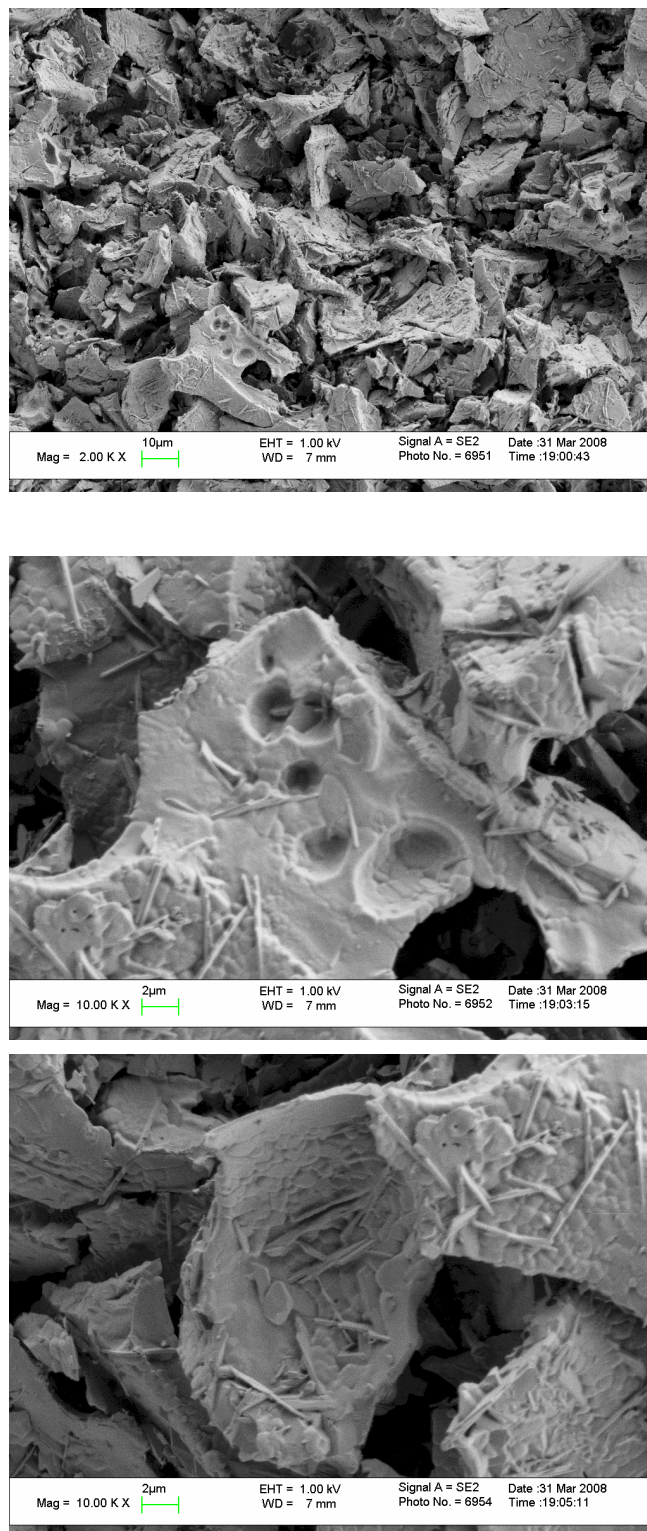
Figure 4.16 Secondary electron SEM images of (a) and (b) 1%Eu, 1%Dy, and 10%B doped SA_2 (c) 1%Eu, 1%Dy, and 20%B doped SA_2

In Figure 4.16, the secondary electron SEM images of the boron doped samples are seen. As a side observation, these images include rod-like structures that the samples without boron do not have. This can be seen by comparing Figures 4.10 and 4.15.

### 4.2.4. SA$_6$: Pure and Different Dopant Amounts

Similar to the SA$_2$ compounds, SA$_6$ samples with different concentrations of Eu and Dy were synthesized. In Figure 4.17, the XRD spectra shows that this particular phase, SA$_6$, was able to accommodate higher concentrations of Eu and Dy, while maintaining the single phase and high crystallinity character. Up to 5 mol% Eu, 5 mol% Dy-doped SA$_6$ powders were synthesized successfully.
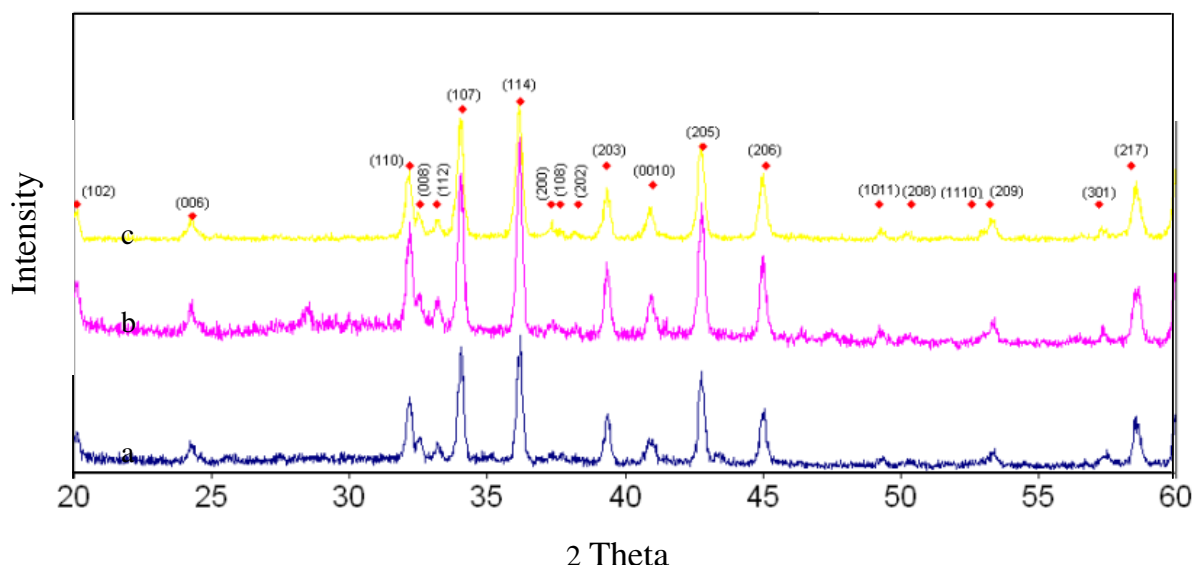
Figure 4.17 XRD spectra of SA$_6$ powders (a) Pure SA$_6$ (b) 1 mol% Eu, 1 mol% Dy-doped SA$_6$ (c) 5 mol% Eu, 5 mol% Dy-doped SA$_6$. The dots represent the JCPDS card No. 10-0066

Using the cathodoluminescence detector on an FE-SEM, the luminescence behavior of the powders was examined for homogeneity of spatial distribution and for correlation to their topography. Figure 4.18 shows the cathodoluminescence and corresponding secondary electron images obtained. The images were acquired from 5 mol% Eu doped and reduced samples of SA$_6$. It can be seen in these images that the smooth surfaces, which were probably hydrated because of the hygroscopic tendency of strontium aluminate powders, did not luminesce, while the fractured surfaces

luminesced strongly. As expected, the hygroscopic nature of the powders decreased their phosphorescence capabilities.
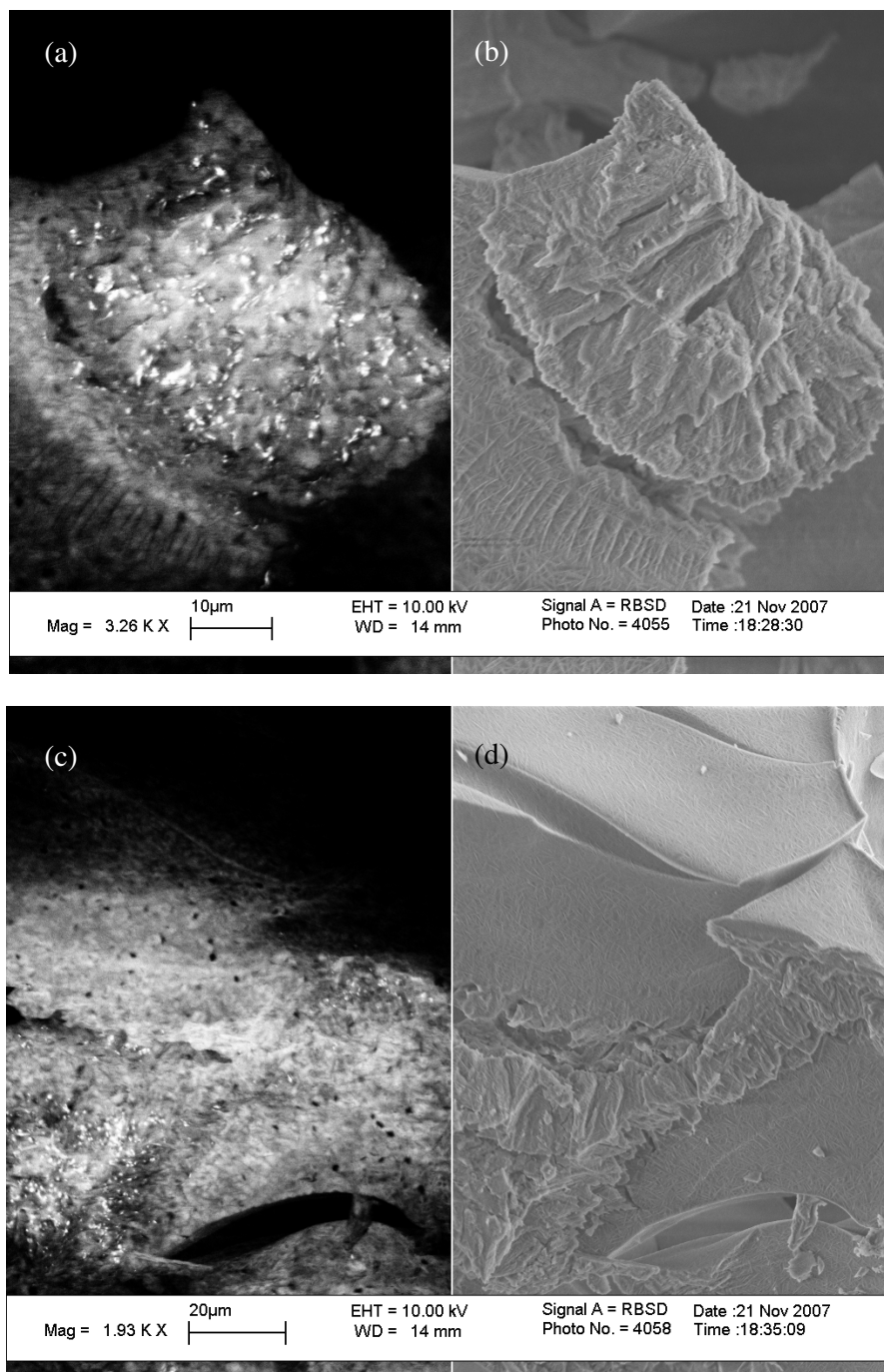

Figure 4.18 (a) and (c) are formed with cathodoluminescence detector, while (b) and (d) correspond to the same part of the powder that they are placed next to, taken with secondary electron detector both as observed in the FE-SEM.

The ELNES were also characterized of the SA_6 powders. Figure 4.19 shows the bright and dark field images for the pure SA_6 compounds, in which the O-K edge and

Al-L$_{2,3}$ edge ELNES strongly resembled those shown in Figure 4.20 and Figure 4.21. That the ELNES remained the same in many measurements across the sample had indicated that the phase purity of the samples remained intact with the doping levels used, of 1 and 5 mol% Eu and Dy. To verify that the same phase was being characterized for each ELNES measurement, EDX measurements were performed from the same locations marked in Figure 4.19, to ascertain the Sr:Al ratio. Typical EDX spectra representative of these samples are shown in Figure 4.22.
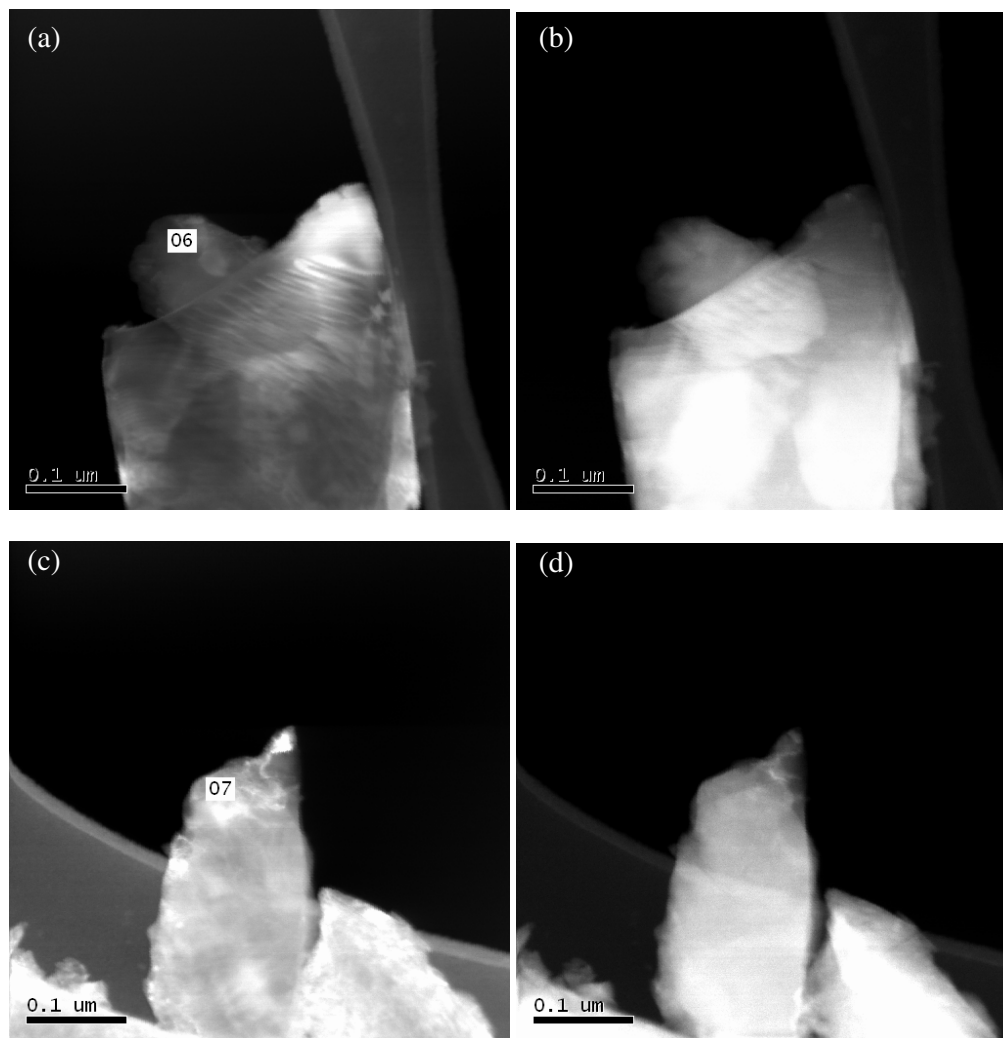
Figure 4.19 (a) and (c) Bright field image, (b) and (d) high angle annular dark field image of 5 mol% Eu and 5 mol% Dy-doped SA$_6$ as observed in the D-STEM
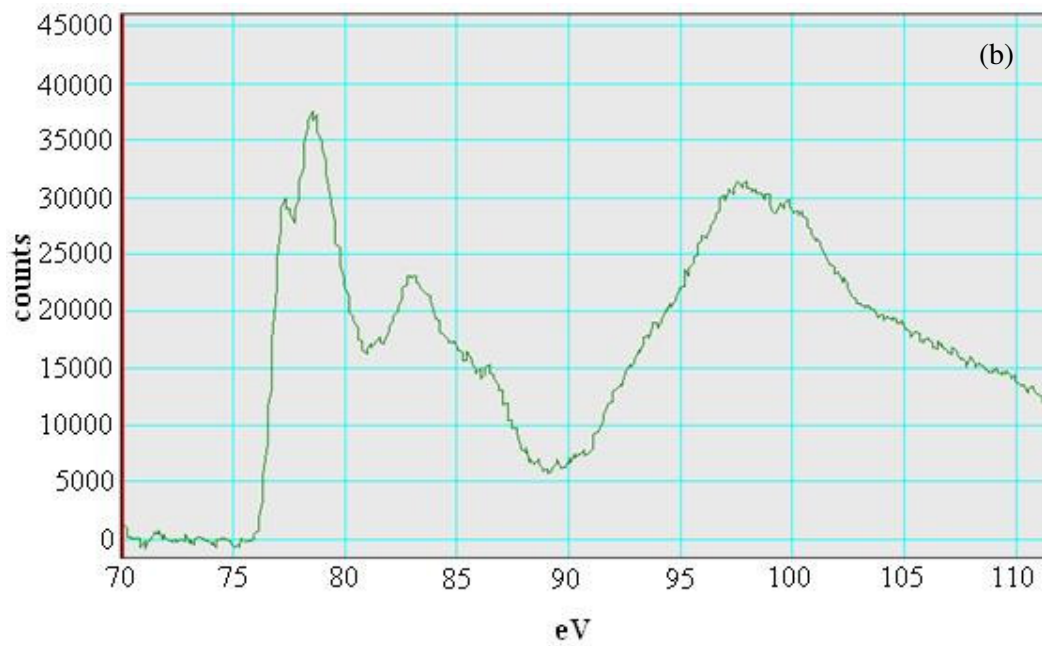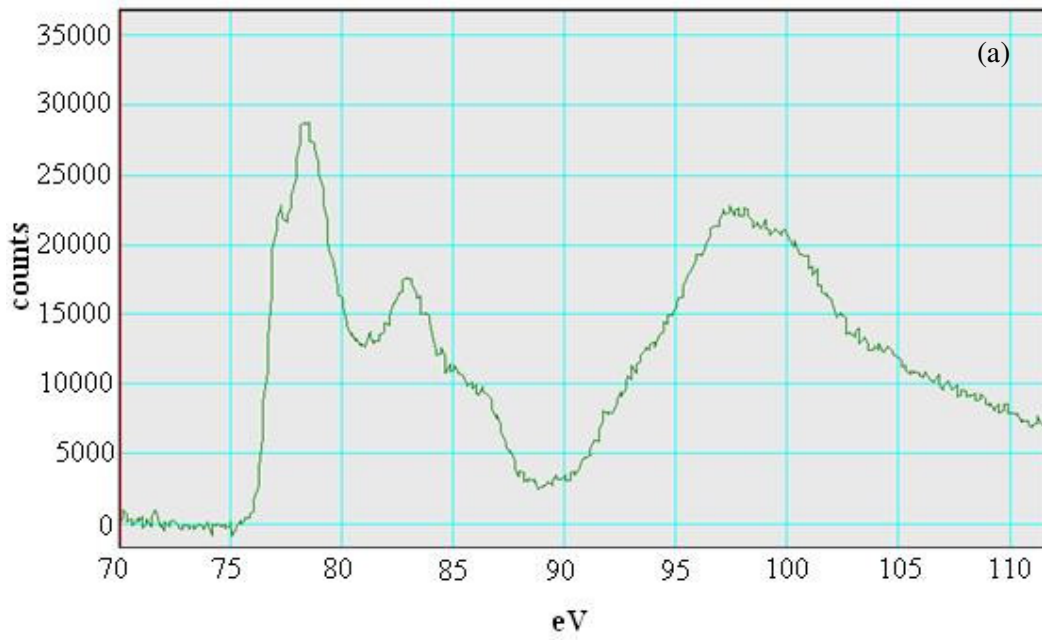
Figure 4.20 Al $L_{2,3}$-Edge ELNES structure of 5 mol% Eu, 5 mol% Dy-doped SA$_6$
measured from the (a) 06 point of the Figure 4.19.a (b) 07 point of the Figure 4.19.c.
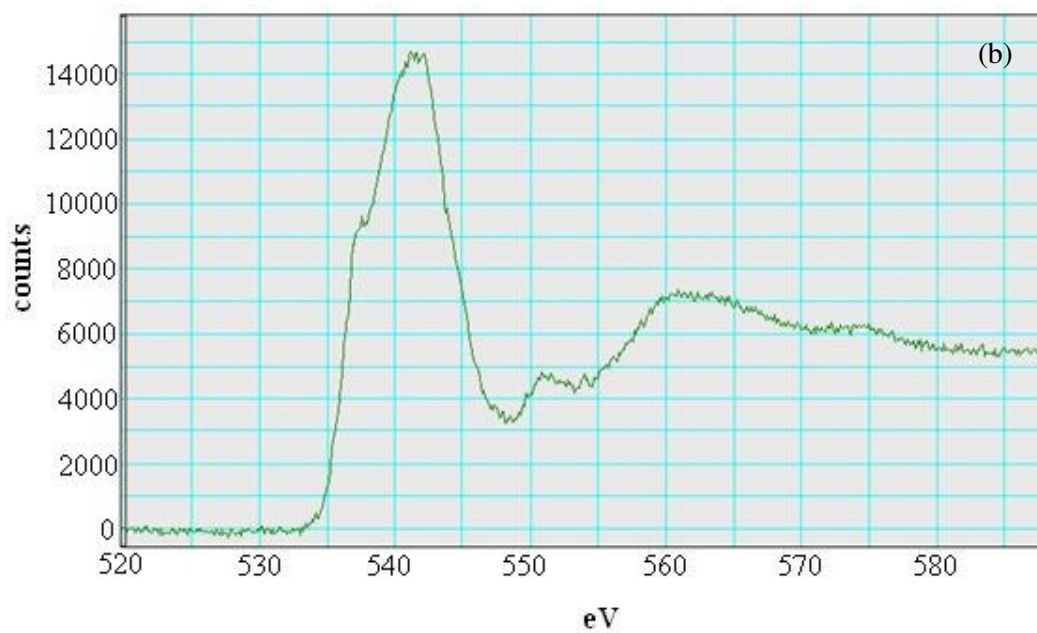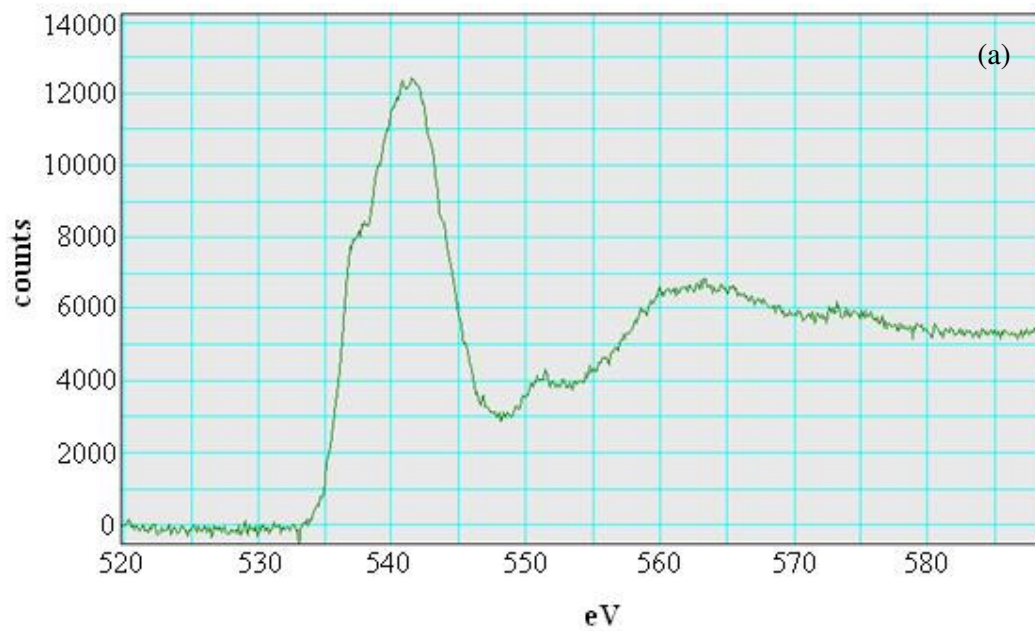
Figure 4.21 O K-Edge ELNES structure of 5 mol% Eu, 5 mol%Dy-doped SA$_6$ measured from the (a) 06 point of the Figure 4.19.a (b) 07 point of the Figure 4.19.c.
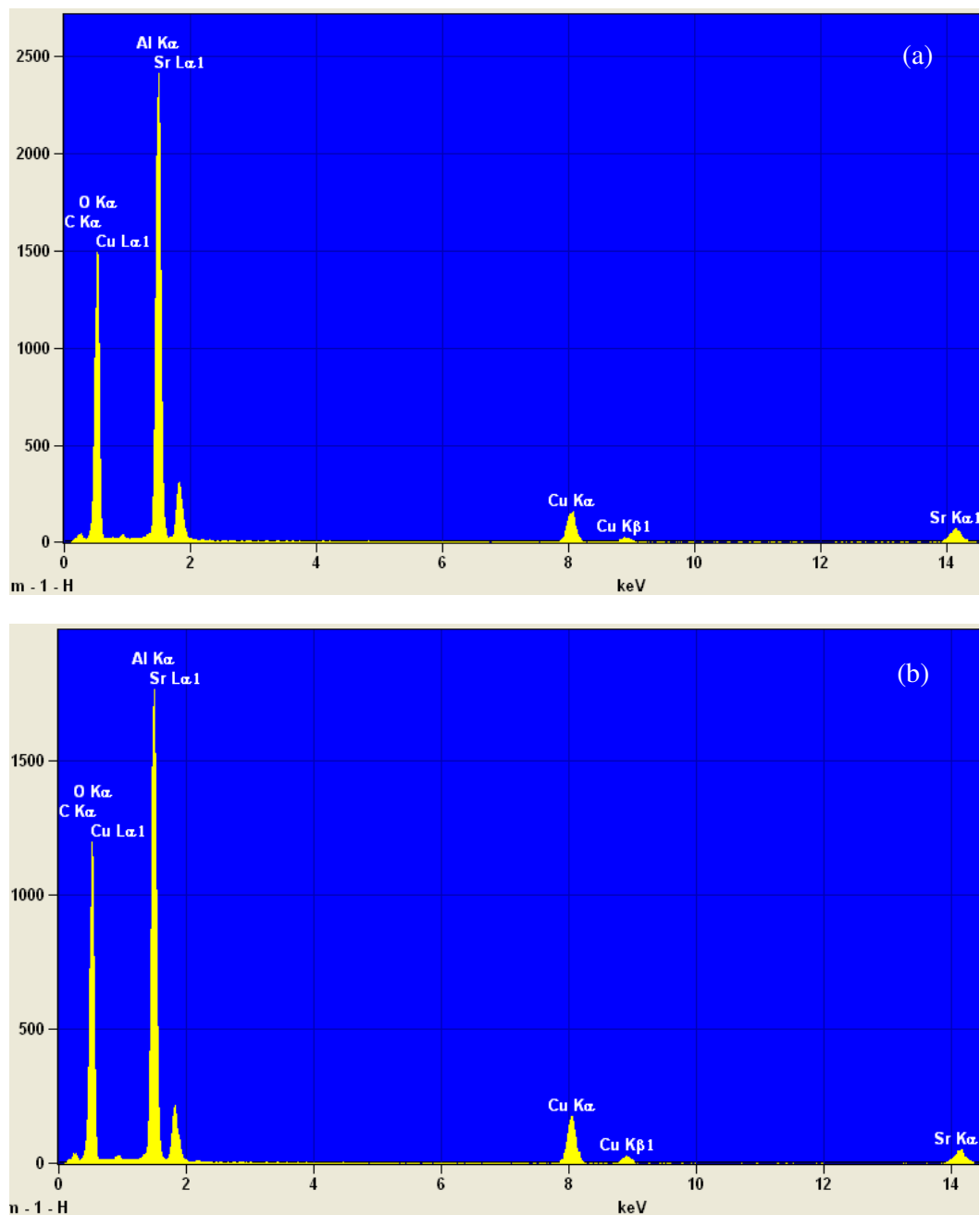
Figure 4.22 (a) EDX measurement of pure SA_6 from the 06 point of the Figure 4.19. (b) EDX measurement of pure SA_6 from the 07 point of the Figure 4.19belonging to pure SA_6.

To study the optical behavior of the various powders, photoluminescence and phosphorescence measurements were carried out at room temperature using UV excitation of λ_{ex} = 325nm. The luminescence spectra were collected using a 200 ms

integration time, while each phosphorescence spectrum was integrated for 20 seconds. Figure 4.23 shows the photoluminescence spectrum of SA_6:Eu^{+3},Dy^{+3}.
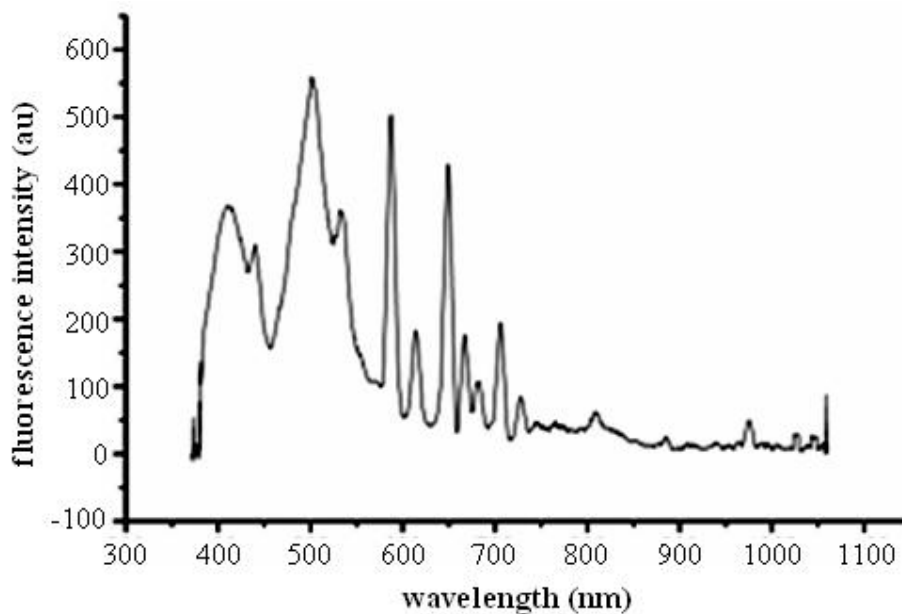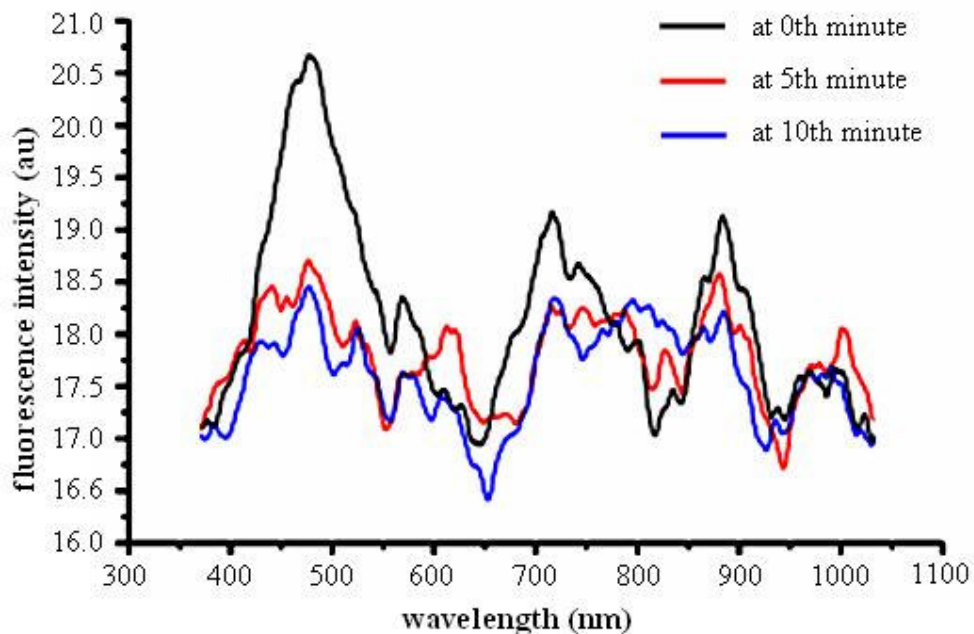

Figure 4.23 Photoluminescence spectrum of SA_6:Eu^{+3},Dy^{+3}

The main peaks had maxima at 432 nm and 519 nm, which corresponded to the emission peaks of SA_6:Eu^{+3},Dy^{+3}, as reported in the literature. The presence of other peaks suggested that there are other sources of emission. The peaks around 633 nm and 667 nm corresponded to the emission from Eu^{+3} ions that have not been incorporated into the host crystal lattice. The other additional peaks may have stemmed from other charge states of the dopant ions.

Figure 4.24 shows the phosphorescence spectrum of the SA_6:Eu^{2+} compound. The emission peak with a maximum at 496 nm indicated that our sample was composed of the $SrAl_{12}O_{19}$:Eu^{+2} phase. Moreover, the presence of only one peak in the spectrum suggested two possible conclusions: the only emission was Eu^{+2} in the structure, and the only phase was $SrAl_{12}O_{19}$:Eu^{+2}.

Figure 4.24 Phosphorescence spectrum of $SA_6:Eu^{2+}$.

The photoluminescence measurements revealed important information about the electronic structure. SA_2 samples doped with 1 mol% Eu, 1 mol% Dy and 10 mol% B emitted red after the visual inspection under the UV of 325nm. This usually indicated that Eu^{3+} has not been fully reduced to Eu^{2+}, because the Eu^{3+} electron transition emits red. Inspection of the samples under UV excitation (265 nm "black light") visually revealed a red glow, suggesting that the powders were not completely reduced due to a problem with the gases. However, when we turned off the UV source, the powders immediately started to phosphoresce green. Since red light has lower energy than green light, this was an interesting paradox, because energy should have been lost during de-excitation of the electron. While performing the PL measurements on this sample, we saw that the luminescence spectra have sharp and high intensity peaks at the red region, as expected, and simultaneously some peaks in the blue-green region, of relatively lower intensity. The higher luminescence intensity in the red appeared to have dominated the green luminescence, and the powders appeared red. However, when the UV excitation source was shut off, phosphorescence was coming from the parts that had been reduced to Eu^{2+}, from which green is emitted. Meanwhile no emission was coming from the Eu^{3+} regions, because they do not phosphoresce. This is a particularly important result, because it is clear evidence that phosphorescence only occurs when Eu^{3+} is reduced to Eu^{2+}. Another conclusion about the state of the powders is that, the

58

reduction had not reached completion. Clearly, the reduction process needs to be improved to maximize the phosphorescence. A final conclusion is that, with the boron-doped samples the phosphorescence brightness was dramatically enhanced, and green emission from the powders was observed for a time-scale on the order of an hour, even though the reduction was not complete.

CHAPTER 5.   CONCLUSIONS

In this study, the synthesis and characterization of phosphorescent strontium aluminates are studied. Basically, a synthesis process was proposed for strontium aluminate compounds with the dopants Eu^{2+} and Dy^{3+} and boron. The proposed method was one step ahead of previous studies as the application of the method was very easy, and the process cost was relatively low. Also, the demand for the lower temperature processing rendered the proposed procedure more cost-effective. The following are the specific contributions of this thesis:

- The first achievement was to synthesize single phase and highly crystalline compounds of strontium aluminates doped with Eu^{2+} and Dy^{3+}. The results were verified by XRD as well as ELNES. For the Eu^{2+}-doped samples for SA_2 showed that the crystal field around the ions had not changed with doping up to 0.67 mol% Eu. This suggested that the crystal lattice of SA_2 was not yet perturbed until a limit of 1 mol% Eu.

- As the production method, the Pechini process was modified as the original Pechini process did not result in the expected single phase and crystalline products. The original Pechini process resulted in the formation of strontium carbonated in the structure, which did not decompose below ~1300˚C. Thus, without preventing the strontium carbonate formation, reducing the temperature would not be possible. Thanks to the modification in the Pechini process, 1000˚C was enough for a successful formation of the desired stoichiometric strontium aluminate compound.

- With the modified Pechini process, the synthesis method is an easy, low-temperature and low-cost method which gains attention among other synthesis methods used by other groups.

- Adding boron to the structure of strontium aluminates during the amorphous precursor preparation resulted in an increase in the crystallinity of the compounds as indicated by the peaks with higher intensities in the XRD. Boron was added to the system successfully up to 30 mol%, which is a new finding in literature. Previously, when boron was added to the system above 20%, amorphous regions were introduced to structure as verified by XRD. However, with the synthesis method that we use, we did not see any amorphous regions upon doping up to 30 mol% of boron. This is important since we do not want to disturb the crystallinity of the material. Boron increases the time of the delayed emission and hence has an important role in the phosphorescence behavior of the strontium aluminate compounds.

- Cathodoluminescence detector was used together with the SEM which showed that luminescence occurred from the rough surfaces of the samples. hygroscopic This is related to the tendency of the strontium aluminate powders. The hydration of the powders reduces their luminescence properties.

- With the boron-doped samples the phosphorescence brightness was dramatically enhanced, and green emission from the powders was observed for a time-scale on the order of an hour, even though the reduction was not complete verified by PL measurements. It was also shown with the PL measurements that phosphorescence only occurred when Eu^{3+} was reduced to Eu^{2+} within the samples.

- EELS showed that the band gap of the strontium aluminate powders that were produced with the modified Pechini process was 6-6.5 eV which is in agreement with literature.

- Finally, ELNES was demonstrated as a possible tool for characterizing the impact of the boron incorporation into the crystal lattice, bringing us one step closer to understanding the relationship between the atomic and electronic structure and the phosphorescence behavior.

CHAPTER 6.   SUGGESTIONS FOR FURTHER RESEARCH

In this chapter, recommendations are presented in order to develop the current study further:

- For the further studies, the synthesis experiments of strontium aluminates should be concentrating on SA_6 instead of SA_2. This is mainly because the SA_6 compound can accommodate higher amounts of dopants into its structure without introducing any amorphous phase and disturbing the crystallinity. Since the main idea of these experiments was obtaining single phase and highly crystalline materials, any disturbances in the crystallinity should be eliminated and thus working with SA_2 has been more difficult.

- We had to conduct ELNES results on very low doping amounts in this study. ELNES obtained for the Eu-doped samples for SA_2 showed that the crystal field around the ions had not changed with doping up to 0.67 mol% Eu. This result suggested that the crystal lattice of SA_2 was not yet perturbed until a limit of 1 mol% Eu. However, this doping amount is very low, and further doping amounts of up to 5 mol% Eu must be characterized by ELNES, as well as doping with up to 5 mol% Dy. The addition of boron to the system may result in higher dopant accommodation in the SA_2 phase, so higher dopant amounts of Eu and Dy along with boron addition must be tried.

- With the addition of boron to the system, the crystallinity had increased, as indicated by the peaks with higher intensities in the XRD. The ELNES measurements must be

performed for samples doped with B up to the point where amorphous regions are observed in the XRD spectra.

- The photoluminescence and phosphorescence measurements are only preliminary up to this moment. The system must be calibrated and more measurements must be performed in order to obtain comparable data. These measurements combined with visual inspection show clear evidence that phosphorescence only occurs when Eu^{3+} is reduced to Eu^{2+}. Figure 6.1 shows the fluorescence spectrum of SA_2 doped with 1%Eu, 1%Dy and 30% B. The peak around 650 nm corresponds to red emission, which is known to come from Eu^{3+} as mentioned in Chapter 2. There are also peaks above 500 nm, which corresponds to the green emission. Visual inspection under UV of 254 nm showed that, during excitation, the color of emission was orange, and when the source was switched off the emission persisted in green. Thus, the powders fluoresce orange-red and phosphoresce green. The conclusion about the state of the powders is that, the reduction had not reached completion. Clearly, the reduction process needs to be improved to maximize the phosphorescence. A final conclusion is that, with the boron-doped samples, the phosphorescence brightness was significantly enhanced, and green emission from the powders was observed for a time-scale on the order of an hour, even though the reduction was not complete.
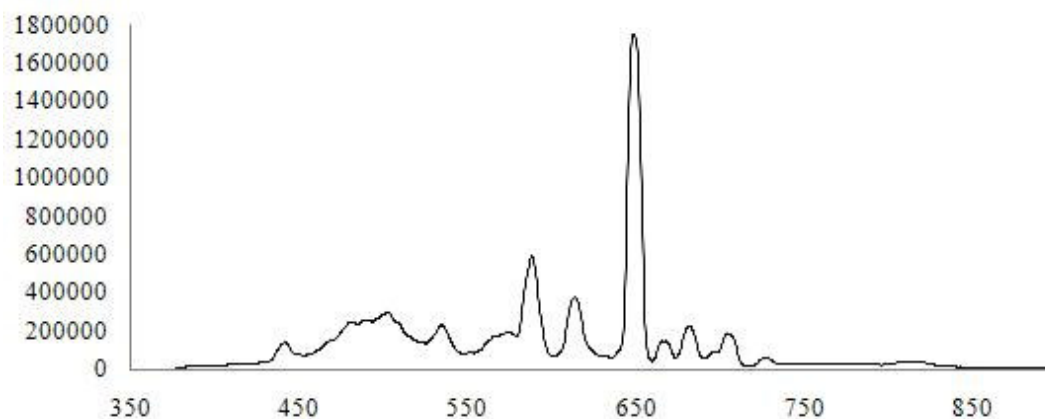

Figure 6.1 Fluorescence spectrum of SA_2:1%Eu,1%Dy,30%B.

- The thermoluminescence measurements are in progress. Thus, combined with the photoluminescence measurements subtle changes in trap state energy levels must be investigated.

- In order to be used as a guide for the next-generation-experiments, energy dispersive x-ray spectroscopy (EDS) and energy-loss near-edge structure (ELNES) measurements of the standards Al_2O_3, Eu_2O_3, Dy_2O_3, SrO and the inspections will be mentioned here.

The SrO particles were very unstable. The particles were observed to be evaporating under the beam very quickly. The Sr $M_{4,5}$ (133eV) edge was tried to be seen with ELNES but this was not successful. Although EDS confirmed the presence of Sr and O elements (and only them), any Sr edge was not seen. Still, the O K (532eV) was measured successfully. The B_2O_3 standard was also tried to be measured. However, after three different solvent trials (water, ethanol, and acetone) it was not possible to see any particles with STEM. The B2O3 standard might be prepared now from its powder state without using any solvent. .

The STEM bright and dark field images and the ELNES results for Al_2O_3 particles can be seen in Figure 6.2 and Figure 6.3, respectively. These might be a starting point for the next generation experiment and measurements.
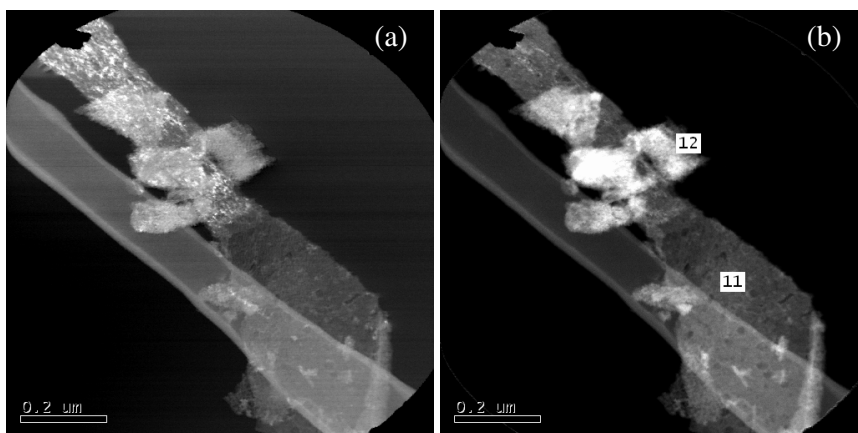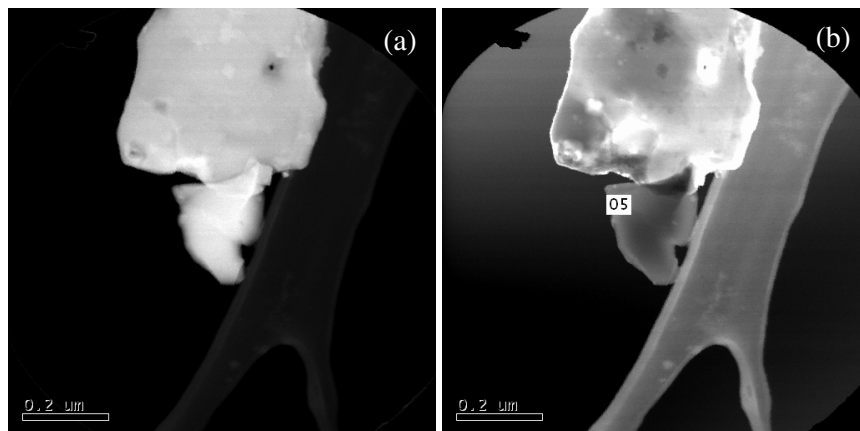

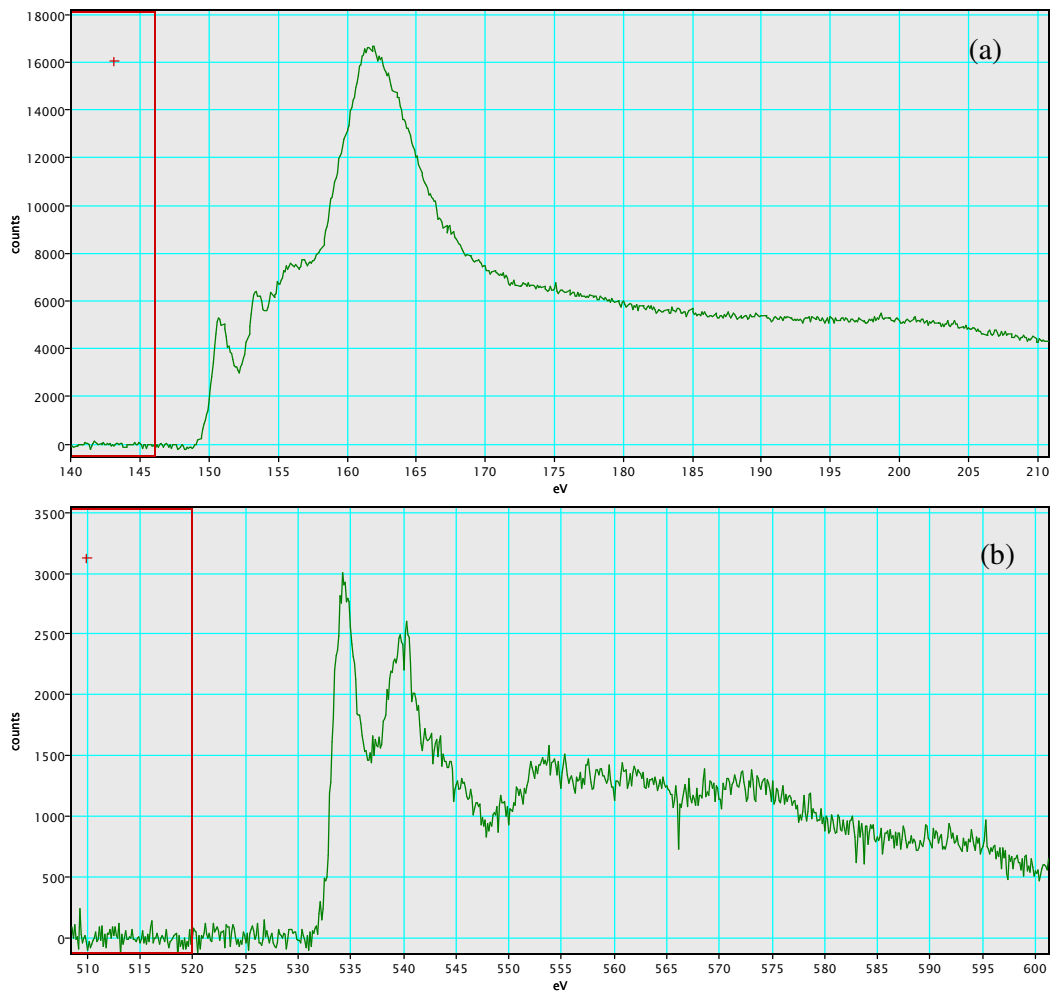**Figure 6.2**(a) Bright field image, (b) high angle annular dark field image of Al_2O_3 as observed in D-STEM
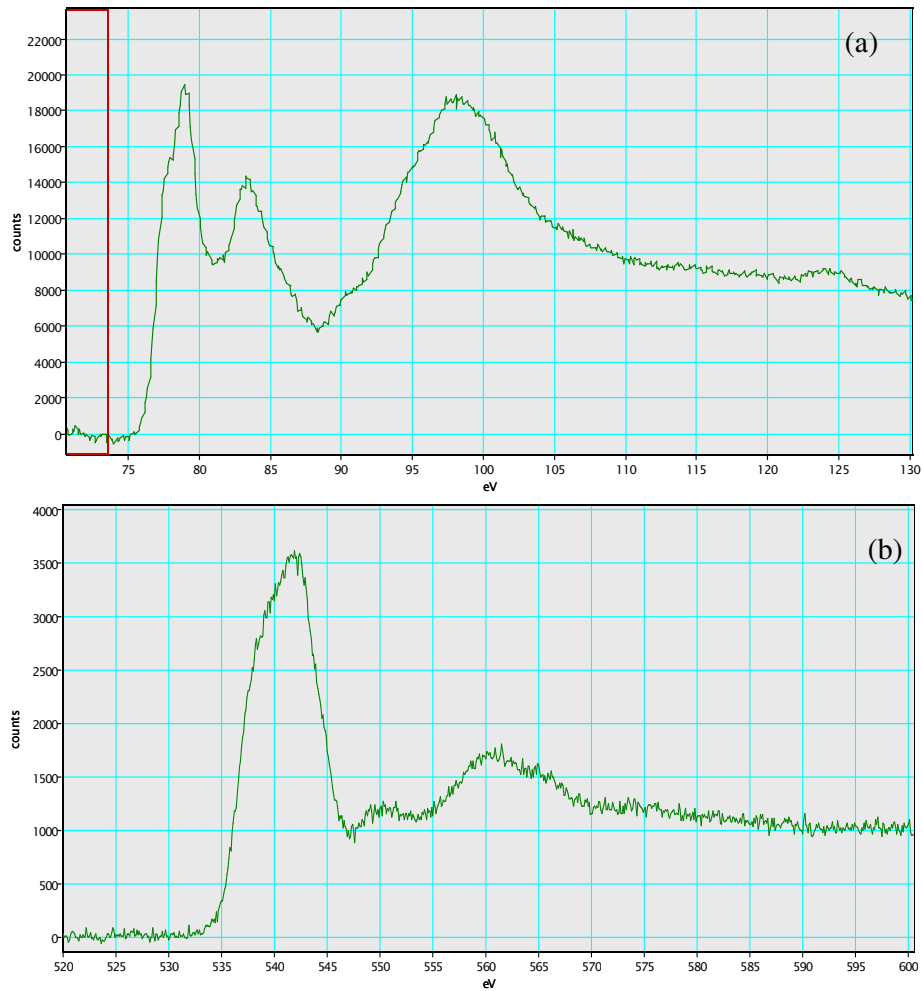
Figure 6.3 ELNES structures of SrO (a) Al $L_{2,3}$-Edge measured from the 11 point of Figure 6.2.b (b) O K-Edge measured from 11 point of the Figure 6.2.b.

The STEM bright and dark field images and the ELNES results for Dy_2O_3 particles can be seen Figure 6.4 and Figure 6.5, respectively.
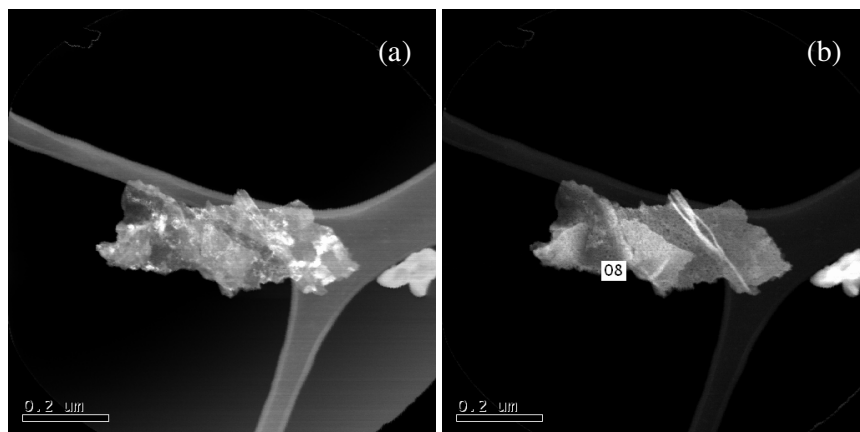

Figure 6.4 (a) Bright field image, (b) high angle annular dark field image of Dy_2O_3 as observed in D-STEM
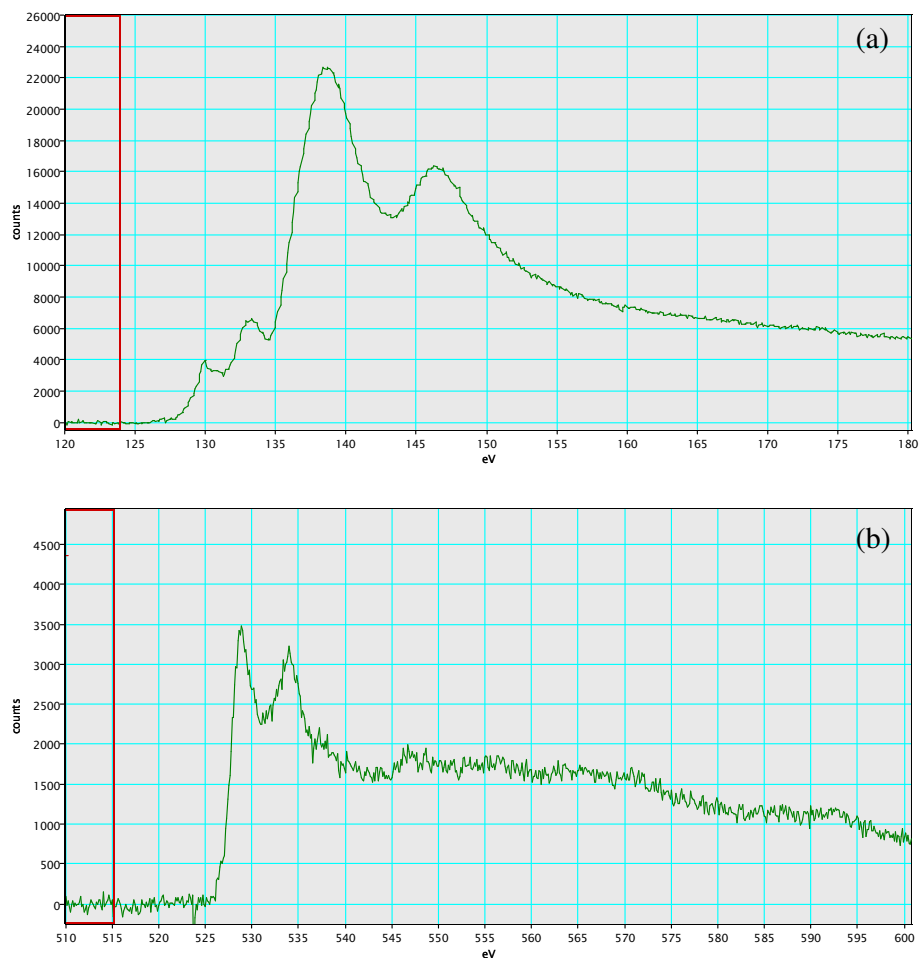
Figure 6.5 ELNES structures of Dy$_2$O$_3$ (a) Al $L_{2,3}$-Edge measured from the 05 point of Figure 6.4.b.(b) O K-Edge measured from 05 point of the Figure 6.4.b.

The STEM bright and dark field images and the ELNES results for Eu$_2$O$_3$ particles can be seen Figure 6.6 and Figure 6.7, respectively.
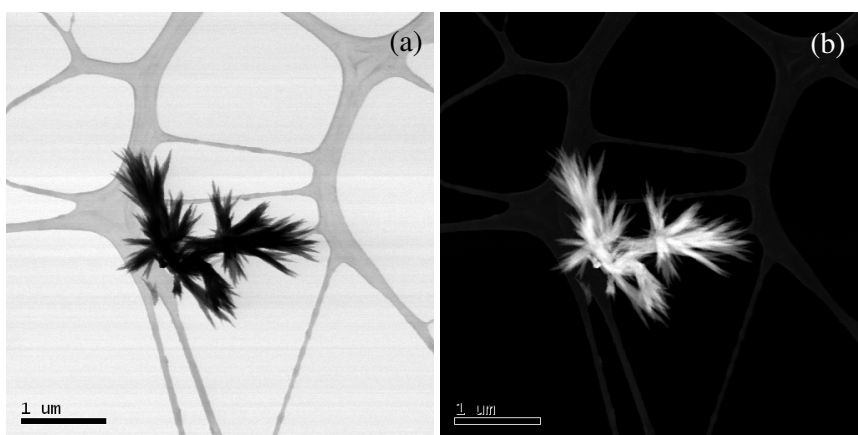

Figure 6.6 (a) Bright field image, (b) high angle annular dark field image of Eu$_2$O$_3$ as observed in D-STEM

Figure 6.7 ELNES structures of Eu_2O_3 (a) Al $L_{2,3}$-Edge measured from the 08 point of Figure 6.6.b(b) O K-Edge measured from 08 point of the Figure 6.6.b.

The STEM bright and dark field images and the ELNES results for SrO particles can be seen Figure 6.8 and Figure 6.9, respectively.

Figure 6.8 (a) Bright field image, (b) high angle annular dark field image of SrO as observed in D-STEM

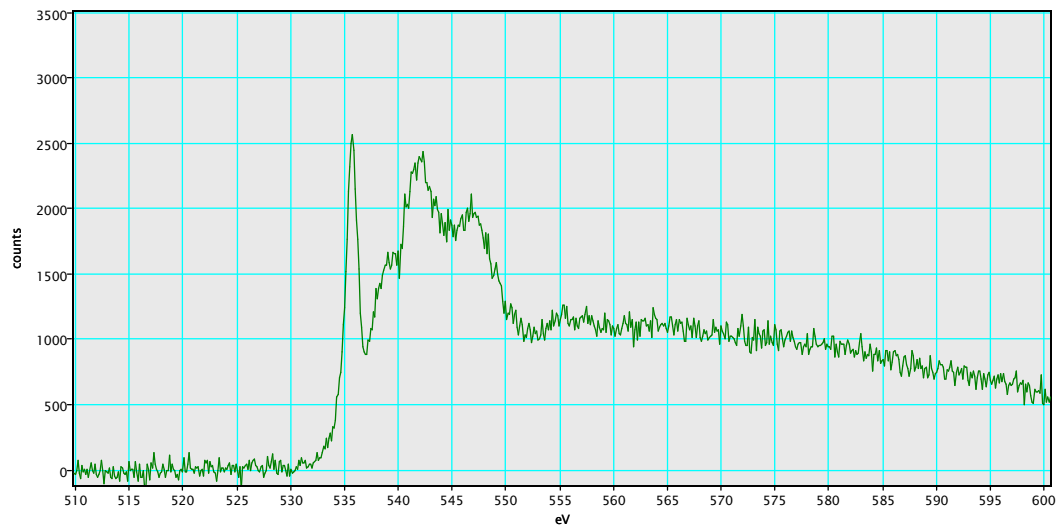**Figure 6.9** O *K*-Edge ELNES structure of SrO measured from a point on Figure 6.8

REFERENCES

1. Katsumata,T., Nabae,T., Sasajima,K., J. Electrochem. Soc., 144, L243, 1997.

2. Matsuzawa,T., Aoki,Y., Takeuchi, N., Murayama,Y., J.Electrochem. Soc., 143, 2670, 1996.

3. Yuan, Z. , Changa,C., Maoa, D., Ying, W., Journal of Alloys and Compounds, 377, 268, 2004.

4. Clabau,F., Rocquefelte,X., Jobic,S., Deniard,P., Whangbo,M.H., Garcia,A., Le Mercier,T., Chem. Mater., 17, 3904, 2005.

5. Holsa,J., Aitasalo,T., Jungner,H., Lastusaari,M., Niitykoski,J., Spano,G., Journal of Alloys and Compounds, 274, 56, 2004.

6. Chang,C., Mao,D., Shen,J., Feng,C., Journal of Alloys and Compounds, 348, 224, 2003.

7. Haranath,D., Sharma,P., Chander,H., Journal of Physics D: Applied Physics, 38, 3871, 2005

8. Hanic,F., Chemekova,T., Udalov,Y., J. Inorg. Chem. (Engl.Transl.), 24, 260, 1979.

9. Nag,A., Kutty,T.R.N., Journal of Alloys and Compounds, 354, 221, 2003.

10. Wang,D., Yin,Q., Li,Y., Wang,M., Journal of the Electrochemical Society, 149, H65, 2002.

11. Niitykoski,J., Aitasalo,T., Holsa,J., Jungner,H., Lastusaari,M., Parkkinen,M., Tukia,M., Journal of Alloys and Compounds, 374, 108, 2004.

12. Ruiz-Gonzales,M.L., Gonzales-Calbet,J.M., Vallet-Regi,M., Cordoncillo,E., Escribano,P., Carda,J.B., Marchal,M., J. Mater. Chem., 12, 1128,2002.

13. Sophya Preethi,K.R., Lu,C., Thirumulai,J., Jagannathan,R., Natarajan,T.S., Nayak,N.U., Radhakrishna,I., Jayachandran,M., Trivedi,D.C., Journal of Physics D: Applied Physics, 37, 2664, 2004.

14. Haranath,D., Sharma,P., Chander,H., Ali,A., Bhalla,N., Halder,S.K., Materials Chemistry and Physics, 101, 163, 2007.

15. Geng,J., Wu,Z., Journal of Materials Synthesis and Processing, 10, 245, 2003.

16. Tang,Z., Zhang,F., Zhang,Z., Huang,C., Lin,Y., Journal of the European Ceramic Society, 20, 2129, 2000.

17. Peng,T., Yang,H., Pu,X., Hu,B., Jiang,Z., Yan,C., Materials Letters, 58, 352, 2004.

18. Singh,V., Gundu Rao,T.K., Zhu,J., Journal of Solid State Chemistry, 179, 2589, 2006.

19. Xu,Y., Lu,P., Huang,G., Zeng,C., Materials Chemistry and Pyhsics, 95, 62, 2006.

20. Capron,M., Douy,A., Journal of American Ceramics Society, 85, 3036, 2002.

21. Pechini,M.P., US Patent 3,330,697, patented 1967.

22. White, M.A., Properties of Materials, Oxford Universtiy Press, New York, 1999.

23. Tilley, R., Colour and the Optical Properties of Materials, John Wiley and Sons, Toronto, 2000.

24. Vij, D.R., Singh, N., Luminescence and Related Properties of II-VI Semiconductors, Nova Science Publishers, New York, 1998.

25. Fox, M., Optical Properties of Solids, Oxford University Press, New York, 2001.

26. Garvie,L.A.J., Craven,A.J., Brydson,R., American Minerologist, 79, p411, 1994.

27. Keast,V.J., Scott,A.J, Brydson,R., Williams,D.B., Bruley,J., Journal of Microscopy, 203, p135, 2001.

28. Ann,C.C., Ed., Transmission Electron Energy Loss Spectrometry in Materials Science and the EELS ATLAS, 2nd Edition, Wiley-VCH, 2004.

29. Gloter,A., Ingrin,J., Bouchet,D., Colliex,C., Physical Review B, 61, p2587, 2000.

30. Köstlmeier,S., Elsasser,C., Physical Review B, 60, p14025, 1999.

31. Scheu,C., Dehm,G., Rühle,M., Brydons,R., Philosophical Magazine A, 78, p439, 1998.